JOURNAL OF PETROLOGY

Journal of Petrology, 2016, Vol. 57, No. 4, 815–838
doi: 10.1093/petrology/egw018
Advance Access Publication Date: 17 May 2016
Original Article

OXFORD

Formation of Plagioclase lherzolite and Associated Dunite–Harzburgite–lherzolite Sequences by Multiple Episodes of Melt Percolation and Melt–Rock Reaction: an Example from the Trinity Ophiolite, California, USA

Nick Dygert[1]*, Yan Liang[1] and Peter B. Kelemen[2]

[1]Department of Earth, Environmental and Planetary Sciences, Brown University, Providence, RI 02912, USA and [2]Department of Earth and Environmental Sciences, Columbia University, Lamont–Doherty Earth Observatory, Palisades, NY 10964, USA

*Corresponding author. Present address: Jackson School of Geosciences, University of Texas, Austin, TX 78712, USA. Telephone: 512-232-5786. E-mail: ndygert@jsg.utexas.edu

Received January 7, 2015; Accepted March 31, 2016

ABSTRACT

Tabular dunite bodies are thought to represent remnants of high-porosity pathways for efficient melt extraction from the mantle. They form by melt–rock reaction, an important physical process that affects the compositions of dunite-hosted basaltic melts and the mantle they originate from. To better understand melt–rock interactions in dunite channels, we analyzed clinopyroxene and orthopyroxene in samples collected across an ~20 m wide dunite–harzburgite–lherzolite–plagioclase lherzolite sequence in the previously well-studied Trinity ophiolite. We found spatial variation and fractionation in minor and trace elements in the constituent minerals. Rare earth element (REE) and high field strength element concentrations increase in unison about 9 m from the dunite–harzburgite contact. Minor elements in clinopyroxene also increase ~9 m from the dunite–harzburgite contact, and NiO contents in olivine increase ~3 m from the dunite–harzburgite contact. Clinopyroxene grains in plagioclase lherzolite samples farthest from the dunite–harzburgite contact exhibit core-to-rim variations in minor and trace elements that mimic the outcrop-scale chemical trends. Collectively, the lithological sequence and major and trace element concentration gradients suggest that a two-stage history of evolution is preserved at Trinity. In the first stage, a cooling melt infiltrated a harzburgitic residue of partial melting, precipitating plagioclase and pyroxene and forming plagioclase lherzolite. In the second stage, a trace element depleted, pyroxene- and plagioclase-undersaturated melt migrated from the dunite channel into the plagioclase lherzolite, forming a hybridized composition by reaction with the plagioclase lherzolite. Because Ni is relatively fast diffusing and compatible in olivine, it was chromatographically fractionated from other trace elements during the infiltration event. Orthopyroxene-saturated melt precipitated new clinopyroxene with depleted major and trace element compositions as it cooled in the dunite, harzburgite, and lherzolite. The REE abundances of the melts in equilibrium with dunite, harzburgite, and lherzolite are similar to those of boninitic dikes that cut crustal units at Trinity, and the infiltrating melts may be genetically related to the dikes. Dunite–harzburgite–lherzolite–plagioclase lherzolite sequences from Trinity and other peridotites probably formed by similar processes. The infiltration of dunite-hosted melts into peridotitic host-rock may be common,

providing an explanation for the wide array of melt–peridotite interactions observed in abyssal peridotites and some ophiolites. This outcrop demonstrates that dunite channels can be sources of melt infiltration as well as melt extraction pathways.

Key words: Trinity ophiolite; melt–rock reaction; dunite channels; plagioclase lherzolite

INTRODUCTION

Tabular dunites are frequently observed in ophiolitic and massif peridotites (e.g. Boudier & Nicolas, 1985). They are tabular, vein-like, or irregular bodies that generally form 5–20% of the mantle section of an ophiolite (e.g. Quick, 1981*b*; Kelemen *et al.*, 1995*a*). Depending on the lithology of the host peridotite, they form dunite–harzburgite, dunite–harzburgite–lherzolite, or dunite–harzburgite–lherzolite–plagioclase lherzolite (DHL–PL) sequences. It is generally considered that dunites are formed by reactive dissolution when olivine-normative basalts percolate through a harzburgite or lherzolite matrix (e.g. Quick, 1981*a*; Kelemen, 1990; Kelemen *et al.*, 1995*a*, 1995*b*, 1997; Asimow & Stolper, 1999; Morgan & Liang, 2003, 2005; Lambart *et al.*, 2009; Van den Bleeken *et al.*, 2010). Dissolution of pyroxene in a partially molten peridotite may lead to the development of reactive infiltration instabilities, resulting in the formation of high-porosity dunite channels for efficient melt extraction from the mantle (e.g. Aharonov *et al.*, 1995; Kelemen *et al.*, 1995*a*, 1995*b*; Spiegelman *et al.*, 2001; Liang *et al.*, 2011; Pec *et al.*, 2015).

Melt flow and melt–rock reaction in the mantle often leave chemical fingerprints in dunites and associated peridotites. Indeed, gradients in major and trace element abundances across and beyond dunite–harzburgite contacts have been observed in spatial geochemical studies of tabular dunites and dunite host-rocks (e.g. Quick, 1981*a*; Obata & Nagahara, 1987; Kelemen *et al.*, 1992; Takahashi, 1992; Takazawa *et al.*, 1992; Varfalvy *et al.*, 1996; Kubo, 2002; Suhr *et al.*, 2003; Braun, 2004; Lundstrom *et al.*, 2005; Maaløe, 2005; Zhou *et al.*, 2005; Morgan *et al.*, 2008; Pagé *et al.*, 2008; Batanova *et al.*, 2011). In many cases, the observed compositional variations have been attributed to interaction between dunite-hosted melt and the dunite host-rock.

A series of studies have investigated compositional variations across DHL–PL sequences at the Trinity ophiolite. Quick (1981*a*) observed significant concentration gradients across a DHL–PL sequence, particularly for TiO_2 in clinopyroxene. Kelemen *et al.* (1992) measured profiles of rare earth element (REE), Ti and Zr concentrations in clinopyroxene for three transects, two extending from tabular dunites and one extending from a pyroxenite into the host-rock. All three profiles show increasing clinopyroxene Nd concentrations away from the dunite or pyroxenite into the host-rock. Lundstrom *et al.* (2005) analyzed three transects across dunite–harzburgite contacts at Trinity, including an ~20 m long DHL–PL sequence originally sampled by Kelemen *et al.* (1992) for Li, B, Nd, and Sr concentrations, and Li isotopes. They observed lower δ^7Li, Li, and B concentrations in dunite and harzburgite increasing to more elevated values in lherzolite and attributed these compositional variations to melt extraction and diffusive interaction of melts across the DHL–PL sequence.

Morgan *et al.* (2008) conducted high-resolution sampling across an ~20 m wide DHL–PL sequence in the Trinity ophiolite at Eunice Bluff [Fig. 1, 41·337573°N, 122·586646°W, previously studied by Quick (1981*a*), Kelemen *et al.* (1992) and Lundstrom *et al.* (2005)] and reported major element abundances in clinopyroxene, orthopyroxene, olivine, and spinel in 44 peridotite samples. They observed concentration gradients in TiO_2, Al_2O_3, Cr_2O_3, and Na_2O in clinopyroxene along the DHL–PL sequence (e.g. Fig. 2a; also see Morgan *et al.*, 2008, fig. 14), with more elevated concentrations in the plagioclase lherzolite and nearly constant, lower concentrations within the dunite, harzburgite, and lherzolite. A gradient in Ni in olivine, offset toward the dunite relative to other major elements, was also observed (Fig. 2b). Gradients of Ni in olivine and Ti in clinopyroxene were shown to be statistically significant after correction for subsolidus re-equilibration. To evaluate their observations, Morgan *et al.* (2008) ran a series of numerical models to investigate concentration gradients generated by melt flow (1) into dunite from the host harzburgite, (2) into host harzburgite from dunite, and (3) with no lateral advection into dunite or host harzburgite. They argued that the major element gradients they measured were produced by the migration of a plagioclase- and pyroxene-undersaturated melt from dunite into host plagioclase lherzolite, as previously inferred by Kelemen *et al.* (1992) based on clinopyroxene trace element data. Thus, tabular dunites do not always drain melt from their host lherzolite and harzburgite. They can act as pathways that facilitate pervasive melt–rock interaction by serving as sources for infiltrating melt. This hypothesis raises the following questions. Under what conditions should we expect dunites to assume the role of a melt source rather than a melt sink? And how do the functions of tabular dunites evolve during mantle upwelling and corner flow? Are there petrological and geochemical trends common to multiple localities that reflect dunite-facilitated melt infiltration into host-rocks?

To address these questions, we measured spatial variations of REE, high field strength elements (HFSE), alkali elements, and transition metal abundances in clinopyroxene and orthopyroxene in samples from the

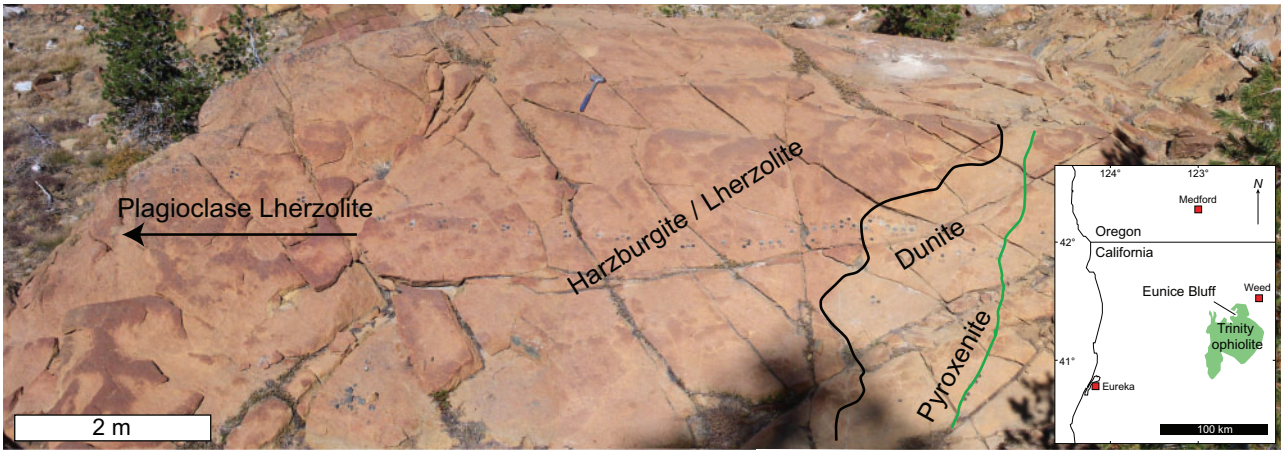

Fig. 1. Field photograph of the traverse investigated in this study. Drill holes produced during sample collection are visible on the outcrop face. The dunite–harzburgite contact is marked in black. Plagioclase lherzolite is outside the field of view; the portion of the outcrop visible here is about 10 m across. A late-stage pyroxenite vein subparallel to the dunite–harzburgite contact is marked in green. Inset shows the location of the Trinity ophiolite.

DHL–PL sequence at Trinity ophiolite studied by Morgan *et al.* (2008). Because of their differing diffusivities and partition coefficients, and lack of 'buffering' by mineral composition and structure, trace elements are more sensitive to melt migration and melt–rock reaction processes than major elements. Our new data allow us to model the formation of plagioclase lherzolite at Trinity ophiolite using both trace and major elements as constraints on melt:rock ratios. We also use the new data to evaluate the specifics of the melt–rock reaction event that formed the DHL–PL sequence, such as composition of the infiltrating melt, its relation to rocks from the crustal section of the ophiolite, and the pervasiveness of melt infiltration. Most significantly, we demonstrate that the dunite at this outcrop represents a source for wall-rock infiltration by migrating melt rather than a melt extraction pathway, in keeping with the results of previous studies (Kelemen *et al.*, 1992, 1995*b*; Morgan *et al.*, 2008), and explore physical scenarios that could facilitate such dunite-sourced infiltration events.

A brief description of Trinity ophiolite

Trinity ophiolite occupies a *c.* 50 km × 75 km section of the Klamath Mountains, northern California. It is a lherzolite-subtype ophiolite (Boudier & Nicolas, 1985) with a relatively thin (~2 km), poorly developed crustal section mostly composed of gabbroic plutons (e.g. Lindsley-Griffin, 1977). Except for small volumes of pyroxenitic and gabbroic dikes, the ultramafic section comprises dunite (15–20%), harzburgite and lherzolite (60–70%), and plagioclase-bearing harzburgite and lherzolite (~15%) (Quick, 1981*a*, 1981*b*). Characteristic of the dunites in the plagioclase lherzolite bearing sections are dunite–harzburgite–lherzolite–plagioclase lherzolite sequences that surround the tabular dunites (e.g. Fig. 1).

Trinity is thought to have formed at a slow spreading center (e.g. Le Sueur *et al.*, 1984; Boudier & Nicolas, 1985; Boudier *et al.*, 1989; Cannat & Lécuyer, 1991) proximal to a subduction zone (e.g. Quick, 1981*a*, 1981*b*; Jacobsen *et al.*, 1984; Brouxel & Lapierre, 1988; Gruau *et al.*, 1991, 1995, 1998; Lindsley-Griffin, 1991; Wallin *et al.*, 1991, 1995; Quick & Gregory, 1995; Wallin & Metcalf, 1998; Metcalf *et al.*, 2000; Ceuleneer & Le Sueur, 2008). The inference of a subduction-related influence is based on observation of relative HFSE depletion and large ion lithophile element (LILE) enrichment in Trinity gabbros and basaltic dikes, isotopic characteristics distinct from mid-ocean ridge basalts, the presence of polygenetic intrusions with ages spanning tens of millions of years, the thin crustal section and poorly developed sheeted dike complex, and the incorporation of subduction-related metavolcanic rocks and trench-related sedimentary basins in the ophiolite.

METHODS

Na, K, Sc, V, Cr, Co, Ni, Sr, REE, Y, Ti, Zr, Nb, Hf, Ta, and Pb were measured in clinopyroxene and orthopyroxene at the Plasma Mass Spectrometry Laboratory, Graduate School of Oceanography, University of Rhode Island by inductively coupled plasma mass spectrometry (ICP-MS) using a Thermo X-series quadrupole ICP-MS system coupled to a New Wave 213 nm laser. Analytical methods are similar to those described by Kelley *et al.* (2003). Natural and synthetic glass standards (ATHO, BCR, BIR, BHVO, GOR 132, KL2, ML3B, St Helens Basalt, T1) were measured at the beginning and end of each analytical session. A range of spot sizes (40–120 μm) were employed depending on grain size and anticipated trace element abundance in the mineral (e.g. Fig. 3g). However, most analyses used 40 or 60 μm spots. We used thick thin sections (*c.* 60 μm) prepared from the 1 inch drill cores used in the study of Morgan *et al.* (2008). Only moderately (≲50%) serpentinized samples were analyzed. Clinopyroxene porphyroclasts are present in the lherzolite and plagioclase lherzolite, but in the

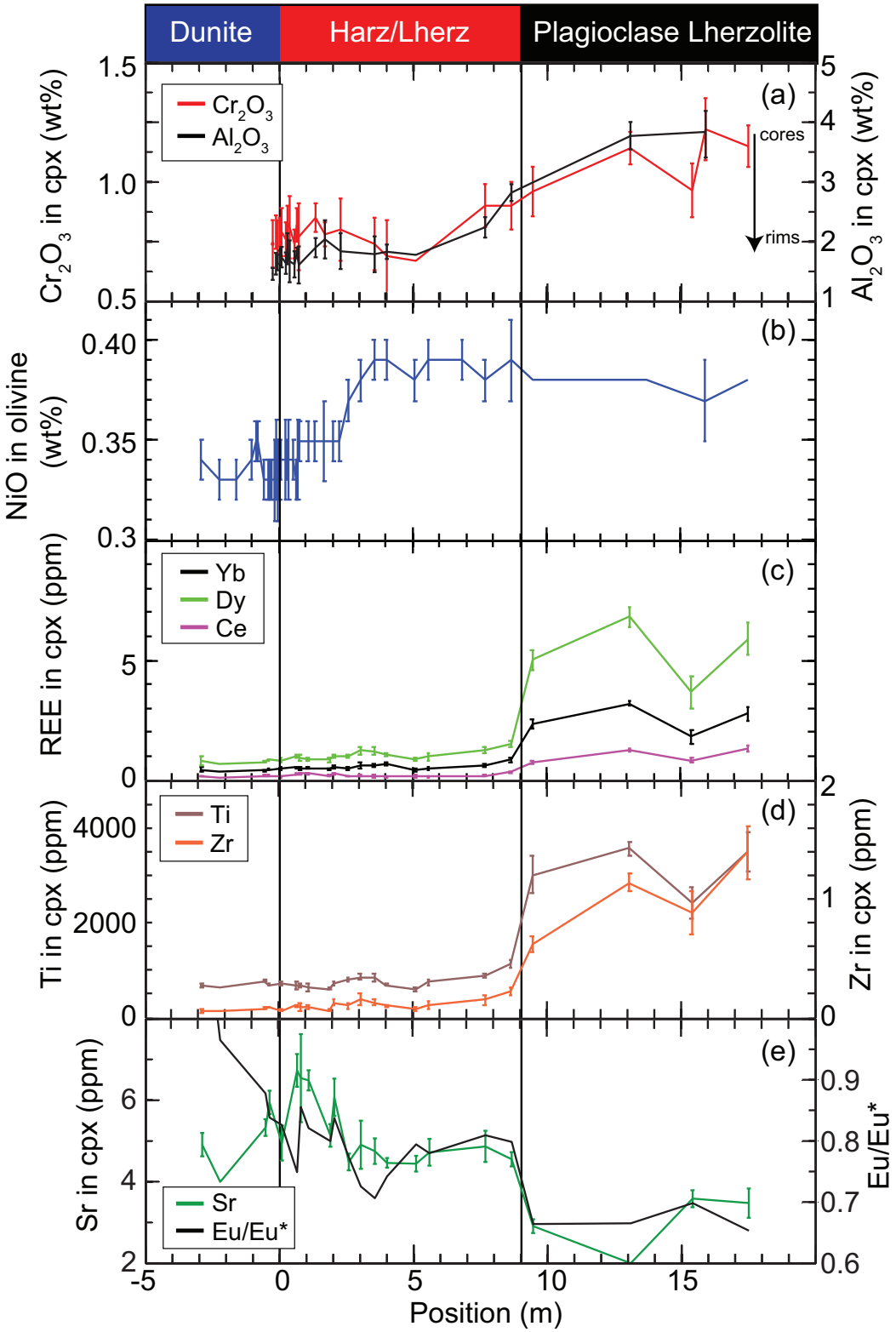

Fig. 2. Variations in selected trace elements and Eu/Eu* (Eu* = Eu/$\sqrt{\text{Sm} \times \text{Gd}}$, where Eu, Sm and Gd are chondrite normalized) in clinopyroxene (cpx) and olivine as a function of distance from the dunite harzburgite contact. (a) Cr_2O_3 and Al_2O_3 in clinopyroxene (Morgan *et al.*, 2008); a few additional data points are included from our LA-ICP-MS analyses; (b) NiO in olivine (Morgan *et al.*, 2008); (c) Yb, Dy, and Ce in clinopyroxene (this study); (d) Ti and Zr in clinopyroxene (this study); (e) Sr and Eu/Eu* in clinopyroxene (this study). The arrow in (a) indicates the range in core–rim compositions exhibited by plagioclase lherzolite clinopyroxene; an example is shown in Fig. 5.

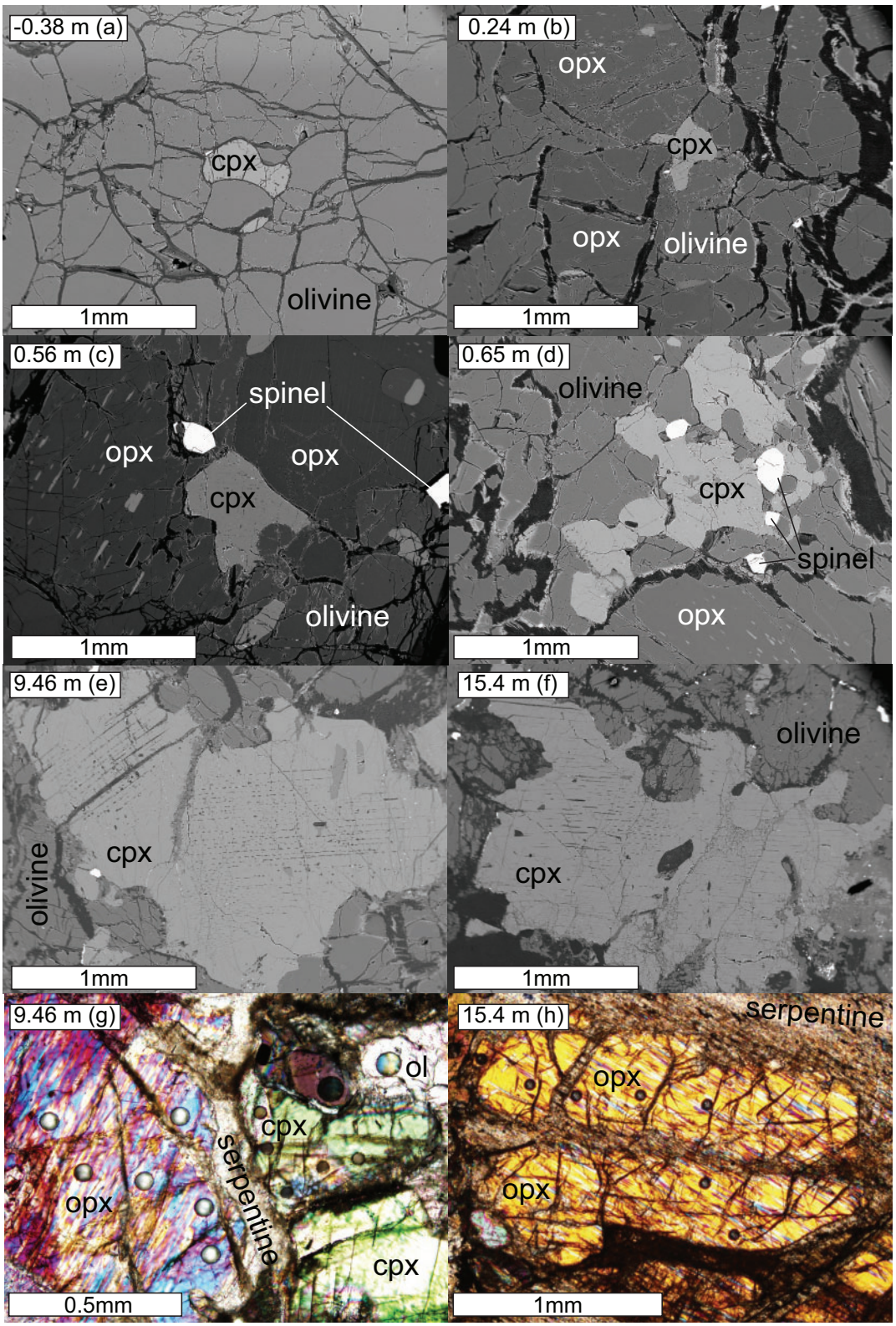

Fig. 3. Backscattered electron and transmitted light micrographs of representative pyroxene grains at different positions across the transect. (a) Clinopyroxene within the dunite; (b–d) clinopyroxene and orthopyroxene within the harzburgite; (e, f) clinopyroxene within the plagioclase lherzolite; (g, h) pyroxenes in plagioclase lherzolite (cross-polarized light). Circles are laser ablation pits. (Note the high-order interference colors, which are a consequence of the thick thin sections.)

dunite (and to a lesser extent in the harzburgite) smaller clinopyroxene grains (~100 μm in diameter, Fig. 3a) are present. These grains were difficult to identify optically so each thin section was mapped using a Cameca SX-100 microprobe at Brown University. Most pyroxenes within and near the dunite are large enough for a single analysis; however, they reach diameters of several millimeters in the plagioclase lherzolite (Fig. 3e and f) and for those larger grains care was taken to place the laser spot as close as possible to the rim and at a range of distances from the grain rim (e.g. Fig. 3g and h). Because of the inherently three-dimensional nature of laser ablation analysis, serpentinized regions and/or phases other than those intended for analysis were occasionally intersected by the laser beam beneath the mineral surface. These compositional anomalies are clearly visible as sudden spikes or dips in the trace element signal and all affected analyses were excluded during data processing.

Counts were converted to concentrations using the Lasy Boy 3.5 Excel macro (Sparks, 2011) using Mg as the internal standard for orthopyroxene and Ca as the internal standard for clinopyroxene. To demonstrate the reproducibility of our data, analyses of the glass standard BIR are reported in Supplementary Data Table 2 from five analytical sessions conducted over a period of 20 months (supplementary data are available for downloading at http://www.petrology.oxfordjournals.org). Measurements are highly consistent with accepted USGS certificate of analysis values using both Mg and Ca as internal standards. Replicate analyses of Trinity peridotite clinopyroxene demonstrate good analytical precision (Tables 1 and 2), with standard deviations ranging from 3 to 33% for single REE and HFSE (1σ). Standard deviations of REE and HFSE analyses average 8 and 12% using Ca and Mg as internal standards, respectively. For orthopyroxene, REE standard deviations are typically <30% except for the light REE (LREE), which have standard deviations of ~50%.

RESULTS

Sample description and petrography

Here we briefly discuss the physical characteristics and textures of pyroxene as a function of distance from the dunite–harzburgite contact [additional sample description has been provided by Morgan (2006) and the Supplementary Material of Morgan *et al.* (2008)]. Backscattered electron (BSE) and transmitted light micrographs of representative pyroxene are presented in Fig. 3. Clinopyroxene crystals are extremely rare in the interior of the dunite but become less scarce near the boundary with harzburgite, reaching a maximum of several grains per thin section at the lithological boundary. Clinopyroxenes in dunite are barely large enough to analyze by laser ablation (LA)-ICP-MS (grains are ~100 μm in diameter; Fig. 3a). Clinopyroxenes in the harzburgite (1–5 vol. %) are considerably more abundant than in the dunite and have larger grain sizes (0·1 μm to 1 mm in diameter; Fig. 3b–d). The maximum clinopyroxene grain size increases across the DHL–PL sequence; grain diameters in plagioclase lherzolite can be 2 mm or more (Fig. 3e and f). These larger grains display orthopyroxene exsolution lamellae that are commonly serpentinized (Fig. 3e and f). Across the traverse, large clinopyroxene grains display lobate olivine embayments (Fig. 3d and f). Smaller clinopyroxenes have tortuous grain boundaries and tend to be interstitial to larger olivine and orthopyroxene grains (Fig. 3a–c). These textures are suggestive of melt impregnation and melt–rock reaction (e.g. Nicolas, 1986; Rampone *et al.*, 1997); however, similar textures can be produced by deformation-induced grain boundary migration (e.g. Mercier & Nicolas, 1975; Dijkstra *et al.*, 2001) as a result of different surface energies (as in poikiloblastic metamorphic textures), or owing to different nucleation and growth kinetics (as in some poikilitic igneous textures).

In general, orthopyroxene crystals are larger than clinopyroxenes; within the harzburgite orthopyroxenes are commonly 1–2 mm in diameter (Fig. 3b–d). Like clinopyroxene, they increase in size across the traverse, reaching diameters of up to 4 mm in the plagioclase lherzolite. They usually have unaltered clinopyroxene exsolution lamellae (Figs 3b–d, g and h). Orthopyroxenes are more serpentinized than clinopyroxenes, especially at their rims (e.g. Fig. 3g and h), which appear 'scooped out' in BSE images. In contrast to clinopyroxenes, orthopyroxenes generally have coherent gradually curving or straight grain boundaries (Fig. 3b–d), although lobate olivine embayments are occasionally observed.

Trace element concentrations

Trace elements were measured in clinopyroxene in 22 samples and in orthopyroxene in 13 samples. The complementary major element dataset has been presented by Morgan *et al.* (2008). Sample averaged trace element abundances in clinopyroxene and orthopyroxene are presented in Tables 1 and 2, and pyroxene rim and core analyses are presented in Supplementary Data Table S1. Primitive mantle normalized concentrations of REE, Y, HFSE, and selected transition metals are shown in Fig. 4a, in which each line represents an average of multiple (core and rim) spot analyses for a thin section. In general, the patterns are smooth and standard deviations are small for clinopyroxene, indicating good reproducibility (larger uncertainties for orthopyroxene are omitted from the figure for clarity but are presented in Table 2 and Fig. 4b). An assessment of the effect of subsolidus re-equilibration on REE distribution in these samples suggests that it is of negligible importance (Supplementary Data Fig. S6, Appendix A; also see Morgan *et al.*, 2008, fig. 16), and thus that the measured concentrations are effectively the same as those in the original magmatic minerals.

Samples are distinguished by their distance from the dunite–harzburgite contact and fall into one of two

Table 1: Trace elements in clinopyroxene

Lithology:	Dunite							Spinel harz					
Sample:	Z01	1σ	Z02	Z04	1σ	Z06	1σ	Z13	1σ	Z18	1σ	Z20	1σ
Position:	−2·89		−2·22	−0·53		−0·38		0·08		0·65		0·79	
n cpx core:	2		1	3		5		12		7		4	
n cpx rim:	—		—	—		—		—		3		—	
Li	—	—	—	—	—	—	—	1·25	—	0·62	0·42	1·00	0·19
Na_2O	0·148	0·041	0·147	0·205	0·017	0·223	0·050	0·212	0·014	0·210	0·015	0·254	0·045
K_2O	—	—	—	0·00137	0·00043	0·00333	—	—	—	—	—	0·00063	0·00030
Sc	100·1	1·2	94·7	111·3	0·4	93·1	5·0	83·2	6·9	87·7	7·8	74·1	7·4
TiO_2	0·114	0·006	0·110	0·129	0·003	0·117	0·004	0·120	0·010	0·117	0·014	0·112	0·007
V	257	19	179	265	10	227	7	201	13	204	20	204	26
Cr	6519	516	4677	5172	358	4805	630	5174	531	5060	302	5181	783
Co	43·8	13·3	21·6	27·5	2·8	19·1	0·6	22·9	2·6	21·6	1·9	21·3	3·2
Ni	516·0	91·3	294·3	292·8	54·7	249·9	6·3	289·9	22·3	292·7	27·5	268·9	36·0
Sr	2·91	0·29	2·00	3·33	0·21	3·95	0·29	2·95	0·43	4·73	0·40	4·54	1·08
Y	4·2	0·5	4·8	4·4	0·2	5·1	0·3	5·1	0·4	6·5	0·4	5·5	0·7
Zr	1·54	0·41	1·27	1·97	0·17	2·28	0·16	1·51	0·19	2·57	0·19	2·37	0·80
Nb	0·0027	—	0·0048	0·0050	—	0·0046	—	—	—	0·0243	0·0195	0·0154	0·0144
La	0·028	0·006	0·015	0·027	0·009	0·037	0·007	0·026	0·005	0·043	0·007	0·039	0·009
Ce	0·171	0·009	0·091	0·163	0·034	0·177	0·021	0·135	0·024	0·230	0·034	0·267	0·049
Pr	0·052	0·001	0·029	0·050	0·013	0·048	0·009	0·039	0·009	0·064	0·013	0·067	0·008
Nd	0·406	0·066	0·284	0·303	0·070	0·341	0·043	0·328	0·059	0·507	0·057	0·479	0·062
Sm	0·193	0·045	0·211	0·165	0·018	0·199	0·028	0·212	0·051	0·297	0·059	0·278	0·032
Eu	0·128	0·036	0·085	0·079	0·019	0·087	0·012	0·089	0·013	0·110	0·017	0·118	0·013
Gd	0·102	0·019	0·100	0·100	0·007	0·109	0·002	0·507	0·056	0·668	0·089	0·631	0·065
Tb	0·525	0·122	0·337	0·454	0·040	0·505	0·033	0·108	0·010	0·133	0·015	0·133	0·020
Dy	0·820	0·186	0·688	0·759	0·023	0·835	0·035	0·827	0·097	0·989	0·081	0·939	0·120
Ho	0·169	0·020	0·177	0·173	0·006	0·198	0·016	0·192	0·019	0·225	0·018	0·215	0·028
Er	0·530	0·087	0·525	0·527	0·061	0·561	0·080	0·581	0·056	0·673	0·082	0·602	0·065
Tm	0·058	0·010	—	0·067	0·006	0·081	0·008	0·084	0·007	0·100	0·008	0·085	0·011
Yb	0·447	0·105	0·346	0·410	0·038	0·446	0·027	0·498	0·069	0·533	0·033	0·504	0·063
Lu	0·050	0·001	0·049	0·045	0·003	0·067	0·005	0·078	0·011	0·089	0·015	0·078	0·010
Hf	0·104	0·033	0·037	0·124	0·035	0·124	0·020	0·087	0·014	0·130	0·020	0·098	0·021
Ta	—	—	0·00383	0·00146	—	0·00076	—	—	—	0·00138	0·00107	—	—
Pb	0·015	0·010	0·002	0·009	0·006	—	—	0·015	0·011	0·050	0·029	—	—

Lithology:	Spinel harz													
Sample:	Z21	1σ	Z27	1σ	Z23	1σ	Z24	1σ	Z25	1σ	Z26	1σ	TP90.11	1σ
Position:	1·08		1·89		2·04		2·58				3·55		4·01	
n cpx core:	4		5		3		4		4		6		1	
n cpx rim:	—		—		—		—		—		4		2	
Li	1·10	0·37	1·19	0·30	0·92	0·18	0·98	0·14	0·91	0·24	1·02	0·27	—	—
Na_2O	0·259	0·031	0·221	0·025	0·270	0·017	0·184	0·016	0·181	0·030	0·209	0·024	0·272	0·081
K_2O	—	—	0·00055	0·00029	0·00071	0·00033	0·00035	0·00016	0·00035	0·00015	0·00113	0·00053	0·00611	0·00496
Sc	69·5	9·4	70·9	6·0	79·5	9·2	68·8	5·0	74·9	10·5	81·3	14·3	70·5	1·8
TiO_2	0·105	0·012	0·105	0·005	0·122	0·009	0·133	0·007	0·144	0·010	0·143	0·013	0·116	0·004
V	198	14	199	20	222	13	212	7	205	17	202	16	169	4
Cr	5143	532	5734	1226	5264	197	4953	444	4804	658	5214	936	4476	125
Co	21·1	1·5	27·0	9·2	21·9	1·8	21·6	2·4	19·6	3·5	23·2	2·0	21·2	0·6
Ni	276·3	19·9	374·3	142·9	285·9	21·3	299·5	31·3	276·1	39·7	346·9	36·4	300·9	21·4
Sr	4·49	0·25	3·18	0·26	4·07	0·46	2·48	0·20	2·91	0·59	2·75	0·31	2·46	0·12
Y	5·0	0·5	4·9	0·5	5·8	0·6	5·7	0·6	7·1	1·1	6·7	1·0	6·2	0·2
Zr	2·28	0·37	1·71	0·21	3·20	0·65	2·56	0·57	3·92	1·26	3·23	0·62	2·49	0·09
Nb	0·0124	0·0045	0·0109	0·0062	0·0117	0·0040	0·0106	0·0028	0·0094	0·0020	0·0102	0·0041	0·0117	0·0037
La	0·037	0·005	0·026	0·008	0·032	0·011	0·018	0·004	0·023	0·006	0·023	0·006	0·022	0·003
Ce	0·258	0·034	0·191	0·018	0·260	0·019	0·156	0·009	0·190	0·013	0·159	0·039	0·134	0·008
Pr	0·066	0·007	0·055	0·004	0·071	0·004	0·050	0·003	0·064	0·008	0·054	0·009	0·048	0·002
Nd	0·464	0·047	0·397	0·069	0·496	0·046	0·427	0·028	0·568	0·054	0·507	0·043	0·438	0·044
Sm	0·284	0·043	0·281	0·045	0·304	0·014	0·310	0·014	0·399	0·026	0·364	0·039	0·307	0·018
Eu	0·113	0·011	0·105	0·007	0·123	0·008	0·119	0·010	0·143	0·010	0·130	0·019	0·118	0·013
Gd	0·124	0·009	0·578	0·043	0·657	0·047	0·703	0·062	0·175	0·026	0·855	0·115	0·766	0·113
Tb	0·612	0·055	0·120	0·021	0·129	0·008	0·135	0·010	0·894	0·089	0·172	0·022	0·142	0·010
Dy	0·845	0·069	0·869	0·121	0·993	0·078	1·011	0·068	1·224	0·161	1·193	0·165	1·059	0·073
Ho	0·207	0·018	0·182	0·017	0·223	0·022	0·226	0·027	0·277	0·040	0·276	0·045	0·248	0·001
Er	0·555	0·053	0·540	0·075	0·631	0·089	0·634	0·045	0·737	0·125	0·776	0·141	0·689	0·089
Tm	0·085	0·005	0·085	0·014	0·096	0·012	0·093	0·013	0·105	0·018	0·104	0·011	0·082	0·014
Yb	0·507	0·051	0·489	0·058	0·563	0·071	0·502	0·064	0·607	0·101	0·599	0·068	0·652	0·063
Lu	0·071	0·005	0·076	0·011	0·081	0·011	0·076	0·006	0·088	0·016	0·094	0·015	0·101	0·008
Hf	0·086	0·016	0·068	0·016	0·150	0·038	0·125	0·028	0·180	0·065	0·195	0·048	0·143	0·014
Ta	0·00037	—	0·00033	0·00027	—	—	—	—	0·00010	—	—	—	0·00121	0·00087
Pb	0·020	0·001	0·026	0·003	0·022	0·014	0·024	0·009	0·015	0·012	0·055	0·051	0·105	0·056

(continued)

Table 1: Continued

Lithology:	Spinel lherz								Plag lherz							
Sample:	TP90.13	1σ	TP90.14	1σ	TP90.16	1σ	TP90.17	1σ	17BK	1σ	18A	1σ	19BK	1σ	1σ19B	1σ
Position:	5·09		5·59		7·68		8·66		9·46		13·1		15·41		17·51	
n cpx core:	3		7		6		5		8		6		13		15	
n cpx rim:	3		7		3		5		7		6		8		9	
Li	—	—	—	—	—	—	—	—	—	—	—	—	—	—	—	—
Na_2O	0·249	0·121	0·321	0·170	0·370	0·144	0·318	0·096	0·248	0·094	0·388	0·051	0·278	0·025	0·387	0·070
K_2O	—	—	0·00825	—	0·01446	0·01156	—	—	—	—	0·00053	—	0·00030	—	0·00069	0·00042
Sc	59·3	3·0	59·3	4·3	61·6	2·5	68·4	3·8	90·6	9·4	88·0	6·4	84·4	5·8	84·7	6·4
TiO_2	0·102	0·007	0·127	0·011	0·149	0·008	0·191	0·016	0·506	0·066	0·593	0·025	0·403	0·052	0·582	0·071
V	187	10	222	14	237	15	262	10	334	23	359	14	284	14	325	20
Cr	5380	387	6069	647	7122	672	7118	534	6304	715	7574	468	6229	893	7239	1071
Co	19·7	1·2	21·4	2·0	22·1	1·6	22·2	1·1	—	—	23·4	1·4	20·4	2·3	19·7	2·0
Ni	321·8	26·9	340·3	34·8	339·9	26·2	366·4	65·1	—	—	322·1	19·1	308·2	43·7	291·5	29·5
Sr	2·44	0·19	2·72	0·33	2·87	0·38	2·55	0·18	0·95	0·22	—	—	1·58	0·21	1·47	0·36
Y	5·2	0·3	5·5	0·6	6·9	0·4	9·0	0·5	29·1	2·4	37·9	1·6	23·3	4·1	37·2	4·5
Zr	1·82	0·41	2·63	0·74	3·81	1·12	5·45	0·76	15·54	1·58	28·49	2·00	22·17	4·44	34·84	5·51
Nb	0·0142	0·0034	0·0174	0·0056	0·0238	0·0044	0·0165	0·0054	0·0168	0·0081	0·0205	—	0·0147	—	0·0170	0·0066
La	0·044	0·022	0·026	0·009	0·029	0·011	0·036	0·006	0·050	0·009	0·084	0·008	0·086	0·010	0·102	0·015
Ce	0·181	0·070	0·157	0·032	0·180	0·039	0·336	0·032	0·736	0·044	1·253	0·087	0·831	0·080	1·300	0·140
Pr	0·042	0·005	0·048	0·008	0·060	0·010	0·102	0·009	0·329	0·042	0·542	0·024	0·310	0·044	0·537	0·057
Nd	0·345	0·041	0·408	0·048	0·555	0·071	0·795	0·074	3·236	0·335	4·805	0·152	2·631	0·394	4·724	0·560
Sm	0·256	0·034	0·286	0·047	0·380	0·032	0·509	0·053	2·036	0·240	2·790	0·156	1·556	0·300	2·690	0·362
Eu	0·103	0·012	0·113	0·012	0·156	0·021	0·201	0·017	0·632	0·057	0·849	0·044	0·484	0·067	0·772	0·089
Gd	0·606	0·071	0·143	0·020	0·902	0·089	1·147	0·076	4·001	0·442	0·914	0·051	0·515	0·096	4·785	0·590
Tb	0·118	0·014	0·681	0·106	0·185	0·018	0·228	0·017	0·746	0·072	5·382	0·278	2·843	0·522	0·851	0·112
Dy	0·862	0·065	0·972	0·155	1·273	0·121	1·524	0·120	4·944	0·477	6·813	0·411	3·657	0·674	5·896	0·673
Ho	0·196	0·016	0·225	0·033	0·280	0·023	0·349	0·024	1·096	0·093	1·456	0·079	0·857	0·150	1·370	0·167
Er	0·521	0·047	0·557	0·085	0·703	0·058	0·994	0·072	2·961	0·287	3·975	0·223	2·201	0·380	3·450	0·436
Tm	0·071	0·004	0·082	0·011	0·100	0·013	0·132	0·016	0·407	0·043	0·568	0·026	0·311	0·053	0·493	0·060
Yb	0·422	0·039	0·482	0·082	0·615	0·069	0·843	0·075	2·350	0·213	3·189	0·089	1·795	0·292	2·765	0·305
Lu	0·074	0·004	0·080	0·015	0·091	0·005	0·122	0·010	0·332	0·040	0·467	0·026	0·282	0·040	0·441	0·052
Hf	0·093	0·036	0·160	0·040	0·214	0·054	0·265	0·049	0·844	0·138	1·237	0·131	0·835	0·208	1·415	0·232
Ta	—	—	0·00045	—	0·00085	0·00067	0·00103	0·00054	—	—	0·00082	—	0·00094	—	—	—
Pb	0·264	0·118	—	—	0·116	0·109	—	—	0·010	0·004	0·007	0·005	0·010	0·005	—	—

Na_2O, K_2O, and TiO_2 are reported in wt %; all other elements are in ppm. Position refers to distance in metres from the dunite–harzburgite contact.

groups: more depleted samples <9 m from the dunite–harzburgite contact (red and black lines in Fig. 4), and more enriched samples >9 m from the dunite–harzburgite contact (blue and magenta lines). Clinopyroxene in samples >9 m from the dunite–harzburgite contact has pronounced negative Sr and notable Eu anomalies owing to the higher partition coefficients for those elements in plagioclase than in pyroxene (e.g. Drake & Weill, 1975; Blundy & Wood, 1994; Bindeman *et al.*, 1998; Wood & Blundy, 2003). Negative HFSE anomalies are present in all clinopyroxene grains, but large positive HFSE anomalies are present in orthopyroxene. Calculated bulk-rock compositions presented in Supplementary Data Fig. S1 (for samples Z26 and Z24, both harzburgites) show that the bulk-rocks do not exhibit HFSE anomalies.

Morgan *et al.* (2008) assumed that the lherzolite–plagioclase lherzolite boundary was ~6 m from the dunite–harzburgite contact. However, this boundary is difficult to discern in thin section and in the outcrop. Instead, trace element patterns of pyroxene can be used to deduce the position of the boundary. Based on the position of the Sr and Eu anomalies (Figs 2e and 4a), we place the lherzolite–plagioclase lherzolite boundary 9 m from the dunite–harzburgite contact.

Figure 4b shows chondrite-normalized REE patterns for pyroxene. All clinopyroxenes exhibit LREE depletion, but those in the plagioclase lherzolite have steeper LREE patterns. Orthopyroxene has REE patterns with fairly constant slopes, but the LREE are scattered owing to larger analytical uncertainty at lower concentrations. Figure 4c compares our analytical results with previous analyses of Trinity samples collected at or near the traverse discussed in this study. The light blue field outlines unpublished plagioclase lherzolite data (Lo Cascio, 2008), the green field encompasses data from Kelemen *et al.* (1992), and the brown field surrounds data from Morgan *et al.* (2008). Collectively, the data show lower REE concentrations in Trinity dunite, harzburgite, and lherzolite, and higher concentrations in plagioclase lherzolite (Fig. 4c).

Spatial geochemical variations

Spatial geochemical variations are present on the grain and outcrop scales. We first discuss outcrop-scale variations. Abundances of Cr_2O_3, Al_2O_3, REE, HFSE, Sr, and Eu/Eu* in clinopyroxene are plotted as a function of distance from the dunite–harzburgite contact in Fig. 2. Transition metal variations (Cr, Sc, V, and Co) are shown in Supplementary Data Fig. S2. Cr_2O_3 and Al_2O_3 in clinopyroxene increase from constant values within the dunite and harzburgite–lherzolite to more elevated values in the far-field plagioclase lherzolite (Fig. 2a). NiO in olivine (Fig. 2b) increases from lower to higher values between 2·2 and 3·6 m from the dunite–harzburgite contact. In contrast, REE, Y, Zr, and Ti (Fig. 2c and d) increase between 8·5 and 9·5 m from the dunite–harzburgite contact. Importantly, there is no spatial offset between LREE and heavy REE (HREE)

Table 2: Trace elements in orthopyroxene

Lithology:	Spinel harz												
Sample:	Z13	Z18	1σ	Z20	Z27	1σ	Z23	Z24	1σ	Z26	1σ	TP90.11	1σ
Position:	0·08	0·65		0·79	1·89		2·04	2·58		3·55		4·01	
n opx core:	1	6		1	2		1	2		4		4	
n opx rim:	—	5		—	—		—	—		2		3	
Li	1·03	—	—	0·29	0·26	0·02	0·27	0·23	0·06	—	—	—	—
Na_2O	—	—	—	0·010	0·007	0·001	0·009	0·012	0·005	0·012	0·008	—	—
K_2O	0·00164	—	—	—	0·00032	0·00025	—	—	—	0·00093	0·00037	—	—
Sc	32·9	39·9	3·6	30·4	31·7	0·5	36·4	33·9	2·9	35·1	1·8	29·6	1·0
TiO_2	0·060	0·083	0·007	0·062	0·060	0·003	0·081	0·0751	0·0003	0·081	0·003	0·062	0·002
V	100	125	7	97	96	7	101	113	5	96	5	92	1
Cr	4253	4744	462	3656	3233	570	3484	3802	687	2933	261	3829	189
Co	70·8	78·3	1·9	58·1	61·1	1·9	56·4	59·8	0·5	58·9	1·9	59·8	1·0
Ni	738	802	29	584	620	31	556	631	7	691	87	719	8
Sr	—	—	—	—	0·014	0·007	—	—	—	—	—	—	—
Y	0·72	0·92	0·13	0·76	0·61	0·11	0·82	0·90	0·19	0·89	0·10	0·66	0·09
Zr	0·20	0·34	0·17	0·24	0·16	0·03	0·34	0·35	0·13	0·35	0·08	0·47	0·21
Nb	0·0187	0·0120	0·0050	0·0195	0·0070	0·0014	0·0075	0·0072	0·0026	0·0064	0·0032	0·0095	0·0028
La	0·0024	0·0027	0·0015	0·0007	0·00041	—	—	—	—	—	—	0·0043	0·0033
Ce	0·0024	—	—	0·005	0·0014	0·0009	0·003	—	—	0·0024	0·0017	—	—
Pr	0·0014	0·0017	0·0013	0·0003	0·00065	0·00046	0·0009	—	—	0·0013	0·0010	0·0013	0·0007
Nd	0·009	0·014	0·013	0·007	0·0019	0·0007	0·010	—	—	0·0058	0·0042	0·0053	0·0029
Sm	0·020	0·0107	0·0046	0·0030	0·0030	0·0001	0·0056	0·0122	0·0097	0·0093	0·0043	0·0054	0·0034
Eu	0·0025	0·0047	0·0025	0·0083	0·0028	0·0015	0·0033	0·0037	0·0024	0·0054	0·0025	0·0029	0·0022
Gd	0·017	0·033	0·017	0·032	0·0253	0·0049	0·033	0·049	0·026	0·0399	0·0080	0·0221	0·0051
Tb	0·0079	0·0096	0·0023	0·0041	0·0059	0·0015	0·0071	0·0112	0·0047	0·0109	0·0031	0·0079	0·0042
Dy	0·077	0·099	0·025	0·078	0·060	0·010	0·085	0·102	0·027	0·109	0·020	0·072	0·015
Ho	0·0239	0·0292	0·0057	0·027	0·0224	0·0043	0·0308	0·032	0·010	0·0340	0·0079	0·0262	0·0062
Er	0·117	0·120	0·020	0·115	0·081	0·012	0·108	0·119	0·020	0·124	0·015	0·095	0·021
Tm	0·020	0·0246	0·0036	0·018	0·0179	0·0012	0·025	0·0245	0·0045	0·0238	0·0032	0·0195	0·0035
Yb	0·130	0·185	0·024	0·160	0·1483	0·0058	0·173	0·1813	0·0078	0·178	0·018	0·160	0·016
Lu	0·035	0·0393	0·0044	0·029	0·0308	0·0018	0·037	0·0352	0·0022	0·0358	0·0026	0·0303	0·0027
Hf	0·011	0·0138	0·0069	0·0053	0·0080	0·0011	0·022	0·021	0·010	0·0190	0·0054	0·021	0·011
Ta	0·00062	—	—	0·00039	0·000156	0·000083	0·00024	0·00060	0·00036	0·00112	0·00061	0·00041	0·00026
Pb	0·0055	—	—	—	0·028	0·003	0·0051	0·0244	0·0006	—	—	0·069	0·050

Lithology:	Spinel lherz						Plag lherz			
Sample:	TP90.13	1σ	TP90.16	1σ	TP90.17	1σ	17BK	1σ	19B	1σ
Position:	5·09		7·68		8·66		9·46		17·51	
n opx core:	1		3		2		3		16	
n opx rim:	2		5		3		3		2	
Li	—	—	—	—	—	—	—	—	—	—
Na_2O	0·038	0·025	—	—	—	—	0·016	0·009	0·034	0·016
K_2O	0·00358	0·00262	—	—	—	—	—	—	0·00046	0·00033
Sc	34·6	2·6	32·2	2·1	35·7	3·0	38·8	1·9	40·7	2·4
TiO_2	0·072	0·002	0·082	0·005	0·158	0·029	0·230	0·014	0·245	0·023
V	91	1	109	4	128	7	181	7	180	18
Cr	3273	95	3637	199	4793	394	5421	500	5649	1139
Co	55·7	0·7	58·9	2·2	57·4	0·6	64·7	0·7	63·9	4·7
Ni	663	20	701	27	682	6	733	15	724	61
Sr	0·070	0·056	—	—	—	—	0·052	0·035	—	—
Y	0·83	0·04	0·81	0·14	1·42	0·45	3·49	0·52	4·10	0·73
Zr	0·48	0·24	0·66	0·37	2·00	0·95	2·69	1·23	3·72	1·08
Nb	0·0052	0·0036	0·0107	0·0067	0·0104	0·0060	—	—	0·0101	0·0053
La	0·0046	—	0·0096	0·0045	0·0028	0·0042	0·0045	0·0029	0·0062	0·0043
Ce	0·013	0·001	0·013	0·011	—	—	0·026	0·021	—	—
Pr	—	—	0·00072	0·00066	—	—	0·0100	0·0070	0·0085	0·0071
Nd	0·0128	0·0067	0·012	0·011	0·018	0·015	0·108	0·086	—	—
Sm	0·0094	0·0011	0·0077	0·0082	0·024	0·011	0·046	0·029	0·057	0·034
Eu	0·0066	0·0033	—	—	0·0069	0·0075	0·022	0·012	0·023	0·015
Gd	0·029	0·027	0·031	0·013	0·067	0·033	0·186	0·074	0·176	0·091
Tb	0·0090	0·0053	0·0084	0·0050	0·016	0·011	0·046	0·024	0·052	0·018
Dy	0·084	0·029	0·096	0·018	0·160	0·062	0·44	0·12	0·46	0·13
Ho	0·0294	0·0043	0·0298	0·0064	0·050	0·011	0·111	0·021	0·148	0·029
Er	0·123	0·013	0·119	0·019	0·196	0·042	0·443	0·051	0·53	0·10
Tm	0·0219	0·0082	0·0246	0·0063	0·0340	0·0038	0·088	0·024	0·104	0·016
Yb	0·184	0·043	0·184	0·020	0·299	0·034	0·647	0·076	0·76	0·11
Lu	0·033	0·011	0·0302	0·0061	0·0555	0·0072	0·1266	0·0091	0·147	0·016
Hf	0·0171	0·0014	0·032	0·017	0·111	0·050	0·136	0·053	0·153	0·053
Ta	0·0033	—	—	—	—	—	0·00097	0·00057	—	—
Pb	0·040	0·026	0·106	0·072	0·053	0·047	—	—	—	—

Na_2O, K_2O, and TiO_2 are reported in wt %; all other elements are in ppm. Position refers to distance in metres from the dunite–harzburgite contact.

concentrations along the transect (Fig. 2c); that is, La and Lu increase from low to high values at the same distance from the dunite–harzburgite contact, similar to the HFSE (Fig. 2d).

Grain-scale concentration gradients are present in plagioclase lherzolite pyroxene (indicated by the arrow in Fig. 2a). An example is shown in Fig. 5. In plagioclase lherzolite samples, concentrations of TiO_2, Al_2O_3, Cr_2O_3,

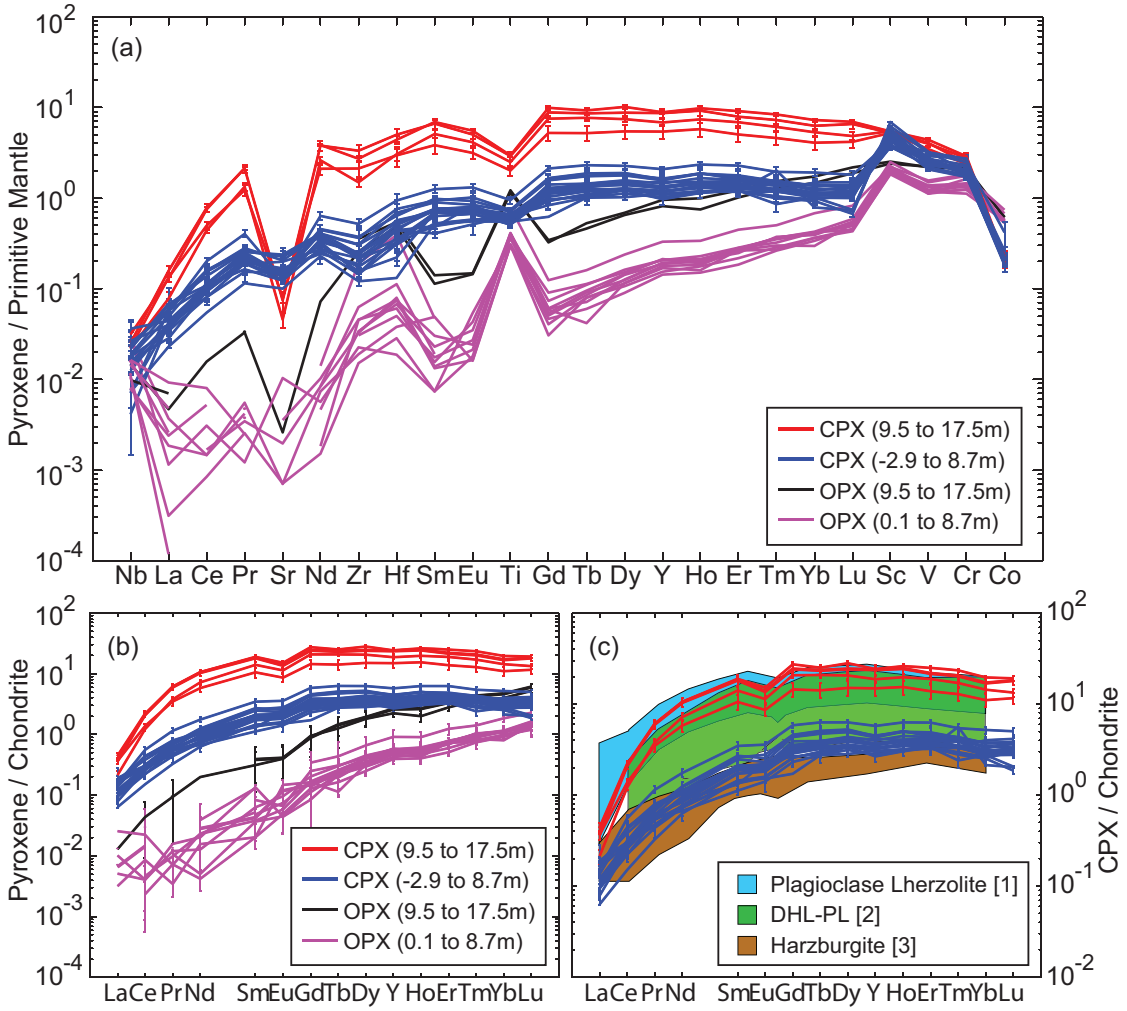

Fig. 4. Sample averaged trace element concentrations in Trinity pyroxenes distinguished by their distance from the dunite–harzburgite contact. (a) Primitive mantle normalized clinopyroxene (red and blue lines) and orthopyroxene (black and magenta lines). Error bars are omitted from the orthopyroxene data to avoid cluttering the figure; uncertainties are given in Table 2. (b) Chondrite-normalized rare earth element patterns for pyroxene. (c) Chondrite-normalized rare earth element patterns in Trinity clinopyroxenes from this study (red and blue lines) compared with ion probe analyses of Trinity clinopyroxenes from [1] Lo Cascio (2008), [2] Kelemen *et al.* (1992), and [3] Morgan *et al.* (2008).

and Na_2O (measured by electron microprobe) are lower in clinopyroxene rims than in cores. These grain-scale concentration gradients mimic the meter-scale gradients observed by Morgan *et al.* (2008); plagioclase lherzolite clinopyroxene rims trend toward compositions of clinopyroxene in the harzburgite. Consistent with these grain-scale minor element variations, REE and HFSE vary from core to rim in the plagioclase lherzolite, with grain rims being more depleted than cores (Supplementary Data Table S1). This is consistent with the Ti zoning pattern determined from microprobe measurements (Fig. 5) and the positive correlation between Ti and REE in pyroxene. Nonetheless, details of trace element zoning in clinopyroxene are difficult to resolve with the spot sizes utilized in our LA-ICP-MS analysis. These grain-scale variations in minor and trace elements are not exhibited by clinopyroxene in the dunite and harzburgite.

DISCUSSION

Characteristics of plagioclase peridotites from Trinity and other ophiolites

Plagioclase-bearing peridotite is commonly observed in ophiolites (e.g. Menzies & Allen, 1974; Quick, 1981*b*; Nicolas & Dupuy, 1984; Takazawa *et al.*, 1992; Rampone *et al.*, 1997, 2008; Borghini *et al.*, 2007; Piccardo *et al.*, 2007; Liu *et al.*, 2010) and in dredged abyssal peridotites from slow spreading centers and fracture zones (e.g. Bonatti *et al.*, 1970, 1992, 1993; Dick, 1989; Elthon, 1992; Girardeau & Francheteau, 1993; Seyler & Bonatti, 1997; Tartarotti *et al.*, 2002; Brunelli *et al.*, 2006; Warren *et al.*, 2009; Brunelli & Seyler, 2010; Dick *et al.*, 2010; Warren, 2016). Many plagioclase peridotites from these tectonic settings have refractory major element compositions (e.g. high Mg# and NiO olivine), elevated incompatible element concentrations, and textures consistent with

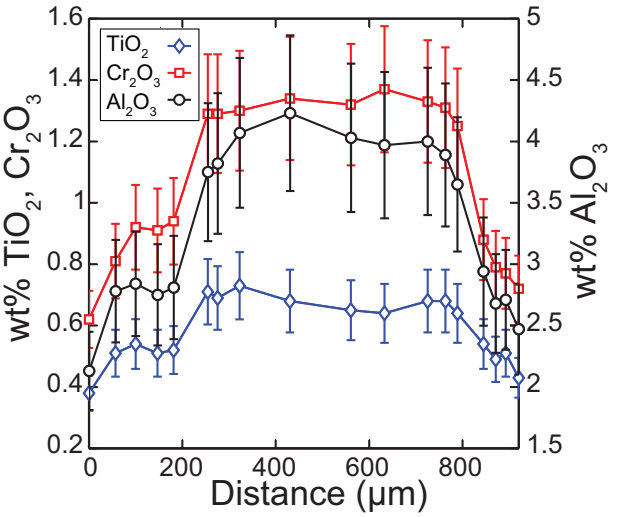

Fig. 5. Core-to-rim minor element concentration variations in a clinopyroxene grain from plagioclase lherzolite (sample TP90.22.8.2.T2; Lo Cascio, 2008). Error bars are estimated uncertainty at the conditions of analysis (15% relative; J. Boesenberg, personal communication). Similar Cr_2O_3 and Al_2O_3 grain-scale concentration gradients can be produced by sub-solidus re-equilibration, but Cr and Al depletion is normally associated with TiO_2 enrichment in plagioclase lherzolites that experience appreciable sub-solidus re-equilibration (e.g. Rampone *et al.*, 1993; Takazawa *et al.*, 1996). The TiO_2 depletion of the clinopyroxene rim suggests that these gradients reflect the composition of the infiltrating melt.

melt impregnation processes (e.g. see review and discussion by Dick, 1989; Collier & Kelemen, 2010; Warren, 2016). The formation of ophiolitic plagioclase peridotite has been ascribed to *in situ* crystallization of plagioclase in undepleted peridotites that experienced limited partial melting (e.g. Menzies & Allen, 1974; Spray, 1982; Bodinier & Godard, 2003; Borghini *et al.*, 2010) or to infiltration of depleted partial melting residues by basaltic melts that crystallize plagioclase and trace element enriched pyroxene (e.g. Nicolas & Dupuy, 1984; Dick, 1989; Bodinier *et al.*, 1991; Elthon, 1992; Kelemen *et al.*, 1992; Niu & Hékinian, 1997; Rampone *et al.*, 1997, 2008; Tartarotti *et al.*, 2002; Borghini *et al.*, 2007; Piccardo *et al.*, 2007; Collier & Kelemen, 2010; Müntener *et al.*, 2010; Saper & Liang, 2014).

REE in clinopyroxenes from Trinity samples are compared with those in plagioclase-free and plagioclase-bearing abyssal and ophiolitic peridotites in Fig. 6a. Middle REE (MREE) to HREE concentrations in Trinity clinopyroxenes are a factor of two greater than in the most enriched plagioclase-free abyssal peridotites. The evolution of Trinity peridotites in a suprasubduction-zone environment, where primitive magmas typically have low HREE and Ti concentrations indicative of extraction from a mantle source depleted in incompatible elements (e.g. Kelemen *et al.*, 2003, 2014), is inconsistent with the presence of an unmodified, fertile plagioclase lherzolite similar to primitive upper mantle. Instead, Trinity plagioclase lherzolite probably formed by basaltic melt impregnation. Trinity clinopyroxene REE concentrations and LREE depletion are similar to those of other ophiolitic plagioclase peridotites (green circles, Fig. 6a). The strong LREE depletion observed in clinopyroxenes in these rocks can be attributed to relatively high plagioclase/clinopyroxene partition coefficients for LREE (e.g. Blundy & Wood, 1994; Bindeman *et al.*, 1998; Wood & Blundy, 2003), combined with the degree of LREE depletion in the impregnating melts that formed the plagioclase peridotites.

Because plagioclase lherzolites at Trinity probably formed by melt infiltration and melt–rock reaction, the calculated trace element contents of melts in equilibrium with plagioclase lherzolite clinopyroxene are not representative of the composition of the infiltrating melt prior to reaction. However, their trace element characteristics can be used to constrain the infiltrating melt composition. In Trinity peridotites, the orthopyroxenes have positive HFSE anomalies, complementary to the negative anomalies in clinopyroxene (compare red and black lines, Fig. 4a). The bulk composition of the plagioclase lherzolite is unknown, but Trinity harzburgite clinopyroxenes show HFSE anomalies similar in magnitude to those in plagioclase lherzolites (Fig. 4a) and have bulk-rock compositions lacking HFSE anomalies (Supplementary Data Fig. S1), suggesting that the infiltrating melt was not depleted in HFSE (e.g. Rampone *et al.*, 1991; Garrido *et al.*, 2000). Finally, the steep LREE depletion in plagioclase lherzolite clinopyroxene suggests that the infiltrating melt was highly LREE depleted.

Formation of Trinity plagioclase lherzolite

Melt impregnation and melt–rock reaction occur in open-system environments with continuous compositional exchange between percolating melts and host peridotite. The formation of LREE-depleted clinopyroxene in plagioclase lherzolite can be modeled with a simple mass-balance calculation that involves reaction and crystallization of a mixture of instantaneous fractional melt of a depleted mid-ocean ridge basalt (MORB) mantle (DMM) source (Workman & Hart, 2005, degree of melting = 8%) and a depleted harzburgite. We evaluate different melt:rock ratios and assume that (1) after a melt infiltration event, melt and residue are in chemical equilibrium, and that (2) re-equilibration and crystallization occurs in a closed system. Major element compositions of the infiltrating melt were calculated using alphaMELTS (Smith & Asimow, 2005) along an adiabat with a potential temperature of 1350°C. For the purpose of illustration we use a depleted melting residue (whose composition was also calculated using alphaMELTS) assuming fractional melting of a DMM source with a potential temperature of 1350°C (degree of melting = 23%). This composition was carefully selected for its low bulk Al_2O_3 and CaO, which are important for forming a mineralogy and composition consistent with the plagioclase lherzolites from Trinity (see inset in Fig. 7 and Table 3).

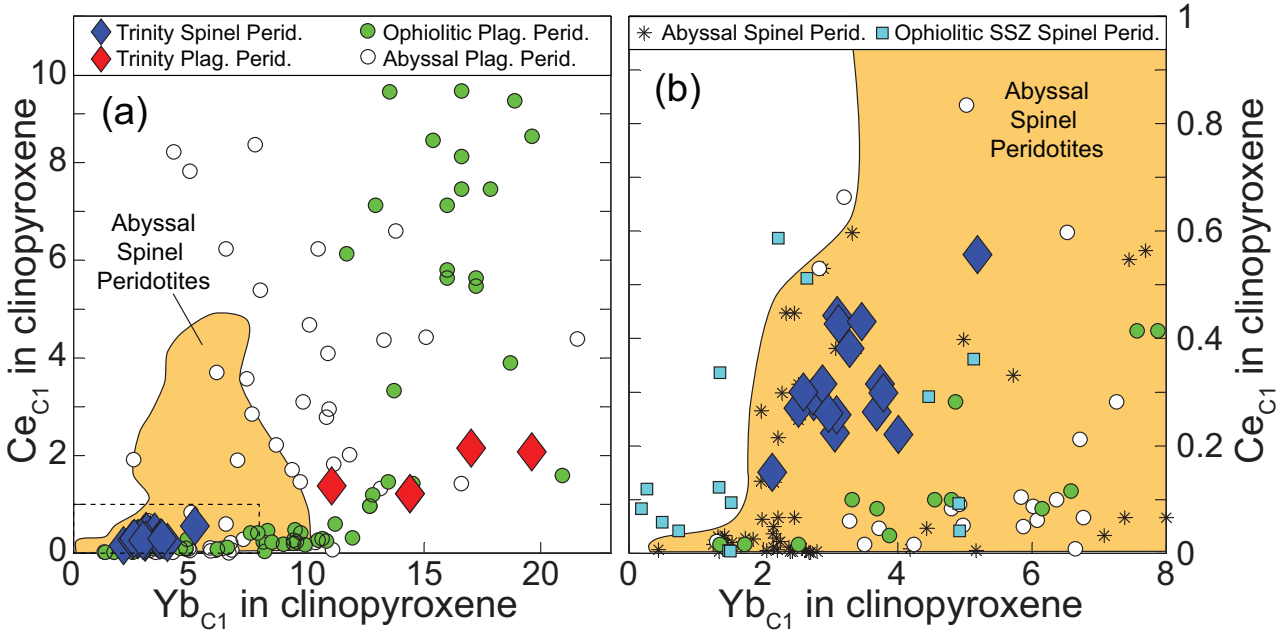

Fig. 6. Chondrite-normalized Ce vs Yb in Trinity clinopyroxene compared with (a) ophiolitic and abyssal plagioclase peridotites, and abyssal spinel peridotites, (b) abyssal spinel peridotites and ophiolitic spinel peridotites from suprasubduction-zone environments. It should be noted that Trinity plagioclase peridotites are similar to other ophiolitic plagioclase peridotites, which generally have higher Yb and higher Yb/Ce than abyssal plagioclase peridotites (a). Clinopyroxenes in Trinity dunite, harzburgite, and lherzolite are similar to those in abyssal peridotites and other suprasubduction-zone ophiolites (b). Data sources: abyssal spinel peridotites: PetDB; abyssal plagioclase peridotites: Brunelli *et al.* (2006), Warren *et al.* (2009), Brunelli & Seyler (2010) and Warren (2016, and references therein); ophiolitic plagioclase peridotites: Barth *et al.* (2003), Rampone *et al.* (2008), Liu *et al.* (2010), Müntener *et al.* (2010) and Guarnieri *et al.* (2012); suprasubduction-zone ophiolites: Bizimis *et al.* (2000), Batanova *et al.* (2011) and Dygert & Liang (2015).

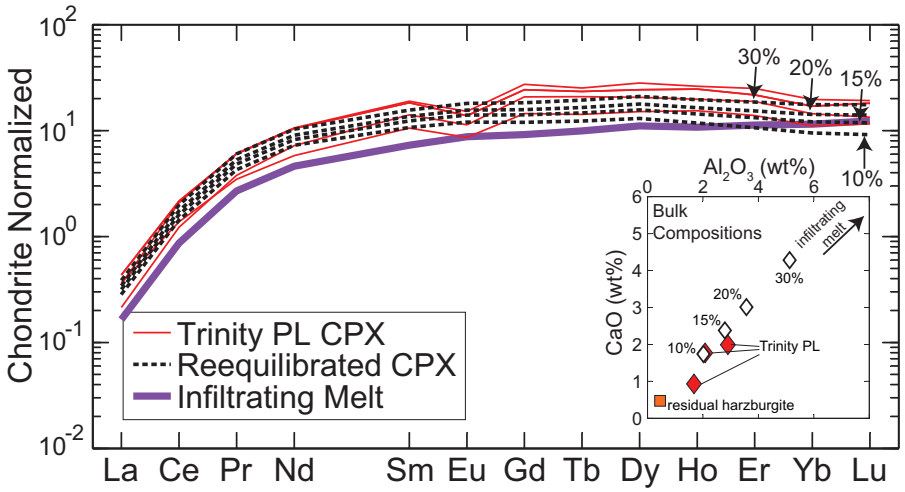

Fig. 7. Results and inputs of the plagioclase lherzolite formation model. Thin red lines are Trinity plagioclase lherzolite clinopyroxene. Purple line is an 8% instantaneous fractional melt of depleted MORB mantle (Workman & Hart, 2005) and black dashed lines are clinopyroxene compositions calculated for mixtures of different proportions of harzburgite and melt. Numbers connected to dashed lines by arrows reflect the volume per cent melt in the mixture. Inset compares CaO and Al_2O_3 contents of Trinity plagioclase lherzolites (red diamonds; data from Quick, 1981*b*) with the model results (white diamonds; numbers indicate per cent melt in the peridotite–melt mixture). The best fit to the trace and major element data is the model with 15% melt, 85% depleted harzburgite.

Models with four effective melt:rock ratios are presented in Fig. 7 (dashed black lines, 10% melt and 90% harzburgite, 15% melt and 85% harzburgite, 20% melt and 80% harzburgite, 30% melt and 70% harzburgite). The success of the models was judged on the consistency of bulk-rock major element compositions with published values for Trinity plagioclase lherzolites (Quick, 1981*b*), and the consistency of trace element concentrations and patterns with those we measured in Trinity clinopyroxene. After calculating the bulk

Table 3: Plagioclase lherzolite formation model

Description:	Trinity Plagioclase Peridotite[1]			Depleted Melting Residue[2]	Infiltrating Melt	10% Melt + 90% Harzburgite Mixture	15% Melt + 85% Harzburgite Mixture	20% Melt + 80% Harzburgite Mixture	30% Melt + 70% Harzburgite Mixture
Sample:	9W20	8W40D	9W2						
Composition									
SiO_2	44.14	43.21	43.22	42.81	49.07	43.44	43.75	44.06	44.69
TiO_2	0.02	0.04	0.06	0.004	0.71	0.075	0.11	0.15	0.22
Al_2O_3	2.9	2.08	1.68	0.46	16.03	2.02	2.79	3.57	5.13
Cr_2O_3	0.36	0.57	0.45	0.71	0.06	0.65	0.62	0.58	0.52
Fe_2O_3				0.08	0.60	0.13	0.16	0.19	0.24
FeO	7.68	8.12	8.91	8.45	7.06	8.31	8.24	8.17	8.03
MgO	42.45	43.77	44.3	46.64	12.66	43.24	41.55	39.85	36.45
MnO	0.12	0.12	0.16	0.17	0.009	0.15	0.14	0.13	0.12
CaO	1.99	1.77	0.95	0.47	13.17	1.74	2.38	3.01	4.28
Na_2O	0.1	0.06	0.05	0.00	0.61	0.061	0.092	0.12	0.18
				REE (ppm)		Calculated REE in Clinopyroxene (ppm)			
La	–	–	–	2.85E-13	0.039	0.067	0.074	0.081	0.091
Ce	–	–	–	7.23E-11	0.52	0.86	0.97	1.06	1.19
Pr	–	–	–	6.38E-10	0.24	0.38	0.43	0.47	0.54
Nd	–	–	–	5.02E-08	2.09	3.29	3.73	4.09	4.65
Sm	–	–	–	1.74E-07	1.07	1.58	1.81	2.01	2.30
Eu	–	–	–	3.38E-07	0.49	0.68	0.79	0.88	1.01
Gd	–	–	–	1.77E-06	1.80	2.35	2.77	3.10	3.61
Tb	–	–	–	6.33E-07	0.36	0.45	0.53	0.60	0.70
Dy	–	–	–	9.75E-06	2.69	3.17	3.81	4.31	5.09
Ho	–	–	–	2.90E-06	0.60	0.66	0.80	0.91	1.09
Er	–	–	–	1.22E-05	1.79	1.69	2.10	2.44	2.96
Yb	–	–	–	6.28E-05	1.86	1.55	1.96	2.31	2.85
Lu	–	–	–	2.15E-05	0.30	0.22	0.29	0.34	0.43
Mineralogy[3]									
Olivine	0.71	0.77	0.78	0.85	–	0.75	0.70	0.66	0.57
Orthopyroxene	0.21	0.16	0.19	0.15	–	0.18	0.20	0.21	0.22
Clinopyroxene	0.038	0.053	0.014	–	–	0.054	0.074	0.092	0.12
Plagioclase	0.046	0.017	0.014	–	–	0.014	0.028	0.045	0.081

[1]Quick, 1981b.
[2]Fractional melting residue of a DMM with a potential temperature of 1350?C. Extent of melting is 23%.
[3]In weight fraction, calculated using alphaMELTS (Asimow & Ghiorso, 1998; Smith & Asimow, 2005) at 2.5kb and reported on a spinel free basis

composition of the melt–peridotite mixture, alphaMELTS (Asimow & Ghiorso, 1998) was used to estimate the mineralogy of the melt–rock mixture at 0·25 GPa. Trace element abundances in olivine, orthopyroxene, clinopyroxene, and plagioclase were calculated using the bulk trace element abundance and the mineral proportions from the alphaMELTS output. Details of the model inputs and results are presented in Table 3.

Modeled clinopyroxene REE are consistent with measured plagioclase lherzolite clinopyroxene REE (compare red and black dashed lines, Fig. 7). The 15% melt model does the best job matching the REE and major element compositions of the Trinity plagioclase lherzolites (see inset in Fig. 7 and Table 3). However, the modeled peridotite has more clinopyroxene than the Trinity plagioclase lherzolite reported by Quick (1981*b*). Because Ca and REE abundances in a mantle melt decrease as extent of melting increases, the infiltrating melt we used represents a compromise that best reproduces the major and trace element compositions, assuming a Workman & Hart (2005) DMM source.

The effective melt:rock ratios we propose are lower than those presented in some previous studies that modeled plagioclase lherzolite formation (e.g. Dick, 1989; Piccardo *et al.*, 2007; Dick *et al.*, 2010). Those previous studies focused on the trace or minor element abundances of the plagioclase lherzolite, and assumed that the mineralogy of the peridotite–melt mixture varies as a function of the plagioclase and pyroxene content of the infiltrating melt based on normative chemistry or petrography. Saper & Liang (2014) demonstrated experimentally that high melt:rock ratios lead to the formation of wehrlites as opposed to plagioclase lherzolites because high proportions of infiltrating basalt lead to crystallization of abundant pyroxene (also see Garrido & Bodinier, 1999). Our model with 30% melt and 70% harzburgite results in an olivine websterite rather than a plagioclase lherzolite. In many cases melt:rock ratios $\lesssim$15% may be most appropriate for modeling the formation of plagioclase peridotites (e.g. Dick, 1989; Elthon, 1992; Piccardo *et al.*, 2007; Rampone *et al.*, 2008; Collier & Kelemen, 2010; Müntener *et al.*, 2010; Saper & Liang, 2014).

The mineralogy of the melt–peridotite mixture has important implications for trace element distribution within the plagioclase lherzolite. Higher melt:rock ratios increase the REE content of the bulk-rock, but they also increase the pyroxene abundance. Our models show that crystallization of additional clinopyroxene buffers the

REE concentrations in clinopyroxene so that they become less sensitive to the melt:rock ratio at higher melt proportions (Table 3). Future efforts to model plagioclase lherzolite formation should take major element compositions and mineralogy into consideration.

Formation of the distinct lithologies and trace element patterns at Trinity

Now we turn to the formation of the DHL–PL sequence and associated concentration gradients, which could be attributed to partial melting, melt–rock reaction, or some combination of the two processes. Partial melting that varies in extent across the DHL–PL sequence can be rejected on physical grounds. The thermal gradient necessary to form dunite by melting and still preserve residual plagioclase lherzolite is unsustainable at geologic timescales (Kelemen, 1990). Lundstrom *et al.* (2005) proposed that diffusive interaction of alkali elements and plagioclase lherzolite adjacent to the dunite lowers the solidus temperature of the mantle around the dunite, leading to a gradient in the degree of melting and melt extraction. However, melting the plagioclase lherzolite would cause increasingly large degrees of LREE depletion not exhibited by clinopyroxene in the dunite, harzburgite, and lherzolite (compare red and blue lines, Fig. 4c), and increased Mg# values in rocks that experienced higher extents of melting when in fact the plagioclase lherzolite olivines have the highest olivine Mg# values (e.g. Morgan *et al.*, 2008, fig. 11).

We propose that the lithological sequence and trace element patterns originate from a two-stage melt–rock reaction process. As discussed in the preceding section, in the first stage extensive infiltration of mantle peridotite, followed by cooling and crystallization, resulted in the formation of plagioclase lherzolite. This may have occurred near the lithosphere–asthenosphere boundary (Fig. 8a) (e.g. Sparks & Parmentier, 1991). In the second stage, pyroxene- and plagioclase-undersaturated melt from a distinct mantle source flowed from the tabular dunite into the plagioclase lherzolite, forming the DHL–PL sequence (Kelemen *et al.*, 1992; Morgan *et al.*, 2008). In this interpretation, the dunite channel formed after the plagioclase lherzolite but during or prior to the second melt infiltration event. We envision that stage two occurred beneath a slow spreading center associated with the formation of the Trinity ophiolite crustal units.

The formation of dunite–harzburgite and dunite–harzburgite–lherzolite sequences in experiments that juxtapose basalt against partially molten harzburgite or lherzolite is well established (e.g. Daines & Kohlstedt, 1994; Morgan & Liang, 2003, 2005; Van den Bleeken *et al.*, 2010; Wang *et al.*, 2013; Pec *et al.*, 2015), consistent with phase equilibrium and petrological models (Quick, 1981*a*; Kelemen, 1990; Kelemen *et al.*, 1992; Asimow & Stolper, 1999). In the above studies the lithological sequences formed by dissolution of pyroxene into pyroxene-undersaturated basalt. Collectively, these results suggest that the lithology and thickness of the distinct mineralogical layers depend on the initial undersaturation of reacting phases in the melt, and the composition of the hybridized melt after melt–rock reaction occurs.

The thick chemical boundary layers at Trinity of ~3·5 m for NiO in olivine and ~9 m for REE, HFSE, Sr, and V suggest that the infiltrating melt advected into the plagioclase lherzolite (Fig. 2; Supplementary Data Fig. S2). Consideration of the mineralogy, grain size, and compositional variations across the DHL–PL sequence constrain the nature of melt infiltration and melt–rock reaction. In addition to the boundary layer thicknesses, important information includes (1) the sharp transition from low to high trace element abundances 9 m from the dunite, and (2) grain-scale compositional gradients that mimic the outcrop-scale concentration gradients (Fig. 5). Important textural information includes (1) residual textures and large grain size of orthopyroxene across the sequence (Fig. 3c and d), (2) clinopyroxenes that show possible melt–rock reaction textures in the harzburgite and lherzolite (Fig. 3c and d), and (3) the increase in clinopyroxene grain size across the transect (Fig. 3). Based on this information, we envision the following mechanism for forming the DHL–PL sequence, illustrated schematically in Fig. 8.

A plagioclase- and pyroxene-undersaturated melt migrated from dunite into a plagioclase lherzolite (Fig. 8c). As it left the dunite, this melt dissolved plagioclase and clinopyroxene in the adjacent peridotite. The melt quickly became orthopyroxene-saturated, leaving residual orthopyroxene in place and forming a harzburgite. Orthopyroxene in the harzburgite diffusively re-equilibrated with the infiltrating melt so that its major and trace element compositions reflected the infiltrating melt composition. Owing to clinopyroxene and plagioclase dissolution, the trace element depleted melt formed a hybridized composition, saturated in clinopyroxene and plagioclase, about 9 m from the dunite–harzburgite contact. The abrupt geochemical front *c.* 9 m from the dunite–harzburgite contact marks the position where clinopyroxenes from the original plagioclase lherzolite protolith remain. The hybridized melt continued percolating past the clinopyroxene saturation front, far into the plagioclase lherzolite. It retained the depleted minor and trace element signature of its source and diffusively interacted with plagioclase lherzolite pyroxene, generating the observed core-to-rim element variations in far-field samples (Fig. 5). Finally, as the peridotite cooled, trapped melts in the harzburgite and dunite precipitated new clinopyroxene (see Kelemen *et al.*, 1992; Tursack & Liang, 2011) reflecting the infiltrating reacted melt composition (Fig. 8d).

Fractionation of trace elements across the DHL–PL sequence

The spatial offset between Ni and incompatible trace elements can be attributed to chromatographic fractionation that occurred as melt percolated from the dunite

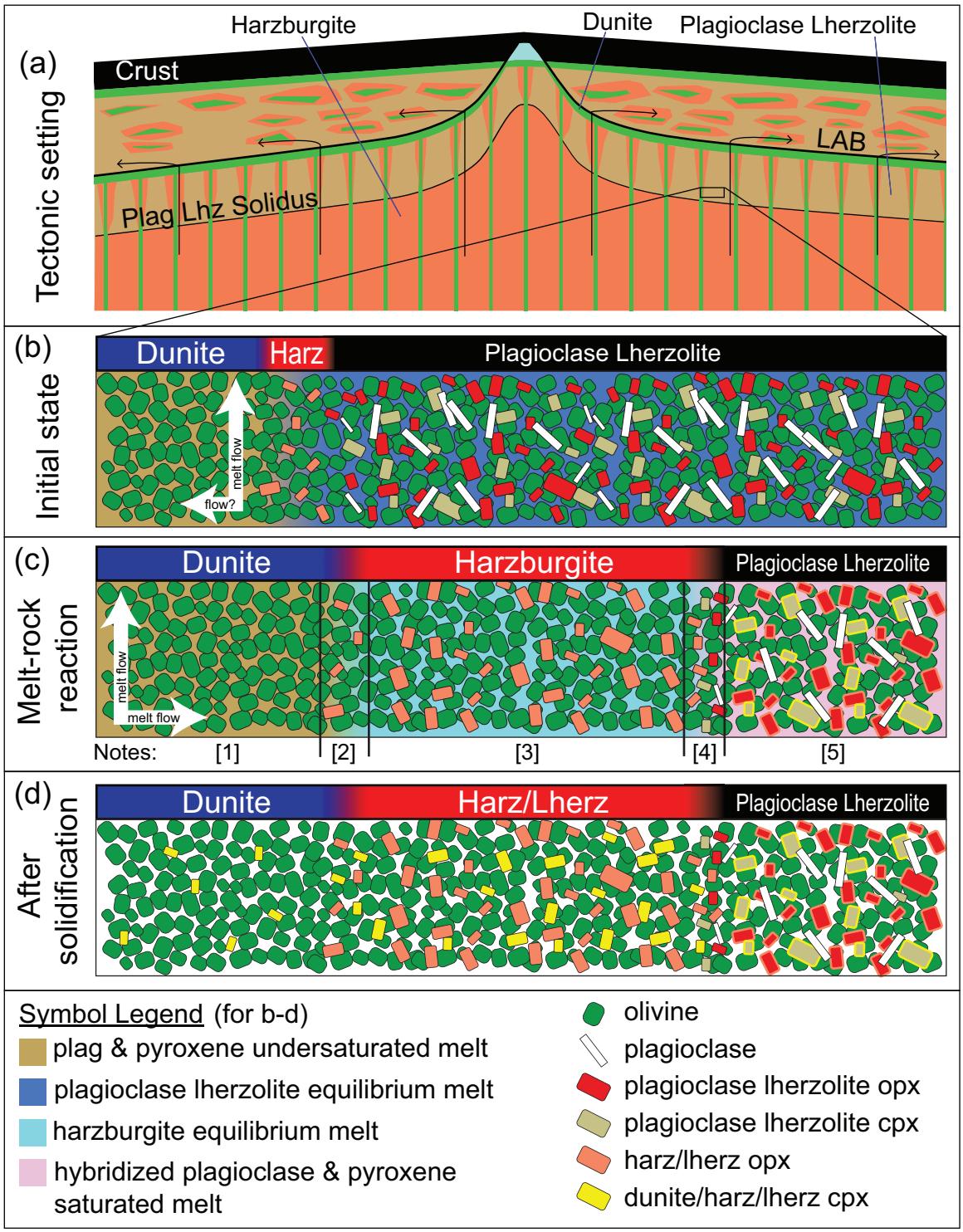

Fig. 8. Schematic illustration of the formation of the DHL–PL sequence. (a) A possible physical setting for the formation of the DHL–PL sequence beneath a slow spreading center between the lithosphere–asthenosphere boundary (LAB) and the plagioclase lherzolite solidus. (b) One potential plagioclase lherzolite–dunite relationship before initiation of melt infiltration. (c) Dunite–harzburgite–plagioclase lherzolite relationship after initiation of melt infiltration. [1] Plagioclase-, orthopyroxene-, and clinopyroxene-undersaturated melt percolating through a dunite channel. [2] Region where orthopyroxene-undersaturated dunite channel-hosted melt percolates into host harzburgite, dissolving orthopyroxene and forming an orthopyroxene-saturated melt. [3] Harzburgite in equilibrium with infiltrating orthopyroxene-saturated melt. [4] Interface between plagioclase lherzolite and harzburgite. Clinopyroxene, orthopyroxene, and plagioclase in plagioclase lherzolite react with infiltrating melt, forming a hybridized clinopyroxene-, orthopyroxene-, and plagioclase-saturated trace element depleted melt. [5] Stable plagioclase lherzolite interacting with hybridized trace element depleted, plagioclase lherzolite saturated melt. Orthopyroxene and clinopyroxene develop trace element depleted rim compositions through diffusive interaction reflecting the composition of the infiltrating melt formed in [4]. (d) Dunite–harzburgite–lherzolite–plagioclase lherzolite sequence formed by melt–rock reaction and cooling. Clinopyroxene in dunite and harzburgite precipitated from pools of trapped melt.

into the plagioclase lherzolite (Morgan *et al.*, 2008). Under conditions of equilibrium exchange between melt and solid, trace elements in a melt advecting through a porous medium will be fractionated owing to solid–melt exchange when the solid and melt are initially out of chemical equilibrium or when the melt mass is changing (e.g. Hofmann, 1972; Prinzhofer & Allègre, 1985; Kelemen, 1986; Navon & Stolper, 1987; Bodinier *et al.*, 1990). A relatively large proportion of melt must migrate through a given region of the matrix to equilibrate a compatible element compared with an incompatible element, which will slow the transport of the compatible element relative to the incompatible element. Assuming that (1) the matrix and melt densities are approximately equal, (2) local equilibration between the melt and solid is instantaneous, and (3) diffusion in the melt is negligible compared with advection, the distance an element front travels through the matrix (L_e) relative to the distance traveled by the melt front (L_m) is given by

$$L_e = L_m\left[\frac{\phi}{\phi + (1-\phi)K_d}\right] \quad (1)$$

where ϕ is the fluid fraction and K_d is the mineral–melt partition coefficient (e.g. Navon & Stolper, 1987). Equation (1) demonstrates that perfectly incompatible elements will be transported at the melt velocity, but infiltration fronts of compatible elements will be slowed considerably. Ni is very compatible in mantle peridotite owing to its high partition coefficient in olivine (~10) and pyroxene (~4), but the trace elements shown in Fig. 2c and d are all incompatible. Thus, it is not surprising that as melt percolated from the dunite into the plagioclase lherzolite the Ni infiltration front lagged behind the incompatible trace elements. Chromatographic fractionation at Trinity will be complicated by the dissolution–precipitation reactions described in the previous sections (e.g. Godard *et al.*, 1995), but our analysis captures the first-order consequences of melt–solid interaction during melt infiltration.

Figure 9 shows the distance traveled by several trace elements (L_e) divided by the distance traveled by Ni (L_{Ni}) for a range of possible values of ϕ calculated using equation (1). This analysis demonstrates that for ϕ <0·02, incompatible trace elements should be strongly fractionated from Ni and one another owing to their differing compatibilities. In the previous description of chromatographic fractionation we assumed instantaneous equilibration between melt and solid, which may not be an unreasonable assumption for fast diffusing elements such as Ni in olivine. In contrast, diffusion rates for REE and Ti in pyroxene are more than three orders of magnitude slower than that of Ni in olivine at mantle temperatures (e.g. Van Orman *et al.*, 2001; Petry *et al.*, 2004; Cherniak & Liang, 2007, 2012). Consequently, solid–melt equilibration of REE and HFSE may be limited by slow grain-scale diffusion in pyroxene. Under such conditions, REE and HFSE will

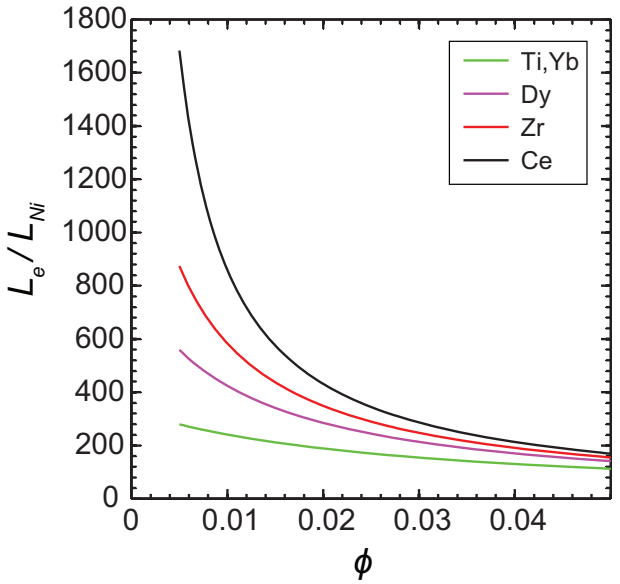

Fig. 9. Length of infiltration front of an element (L_e) recorded in a solid matrix divided by the length of infiltration front of Ni (L_{Ni}) for selected incompatible trace elements with a range of compatibilities as a function of melt fraction (ϕ). Partition coefficients (K_d) used here were calculated for a Trinity harzburgite (17% orthopyroxene, 83% olivine) and are as follows: Ni 8·9; Ti and Yb 0·27; Dy 0·011; Zr 0·0052; Ce 0·00026.

advect through the plagioclase lherzolite at effective velocities close to the melt velocity, and no chromatographic fractionation will be observed. Clinopyroxenes in Trinity harzburgite crystallized directly from the infiltrating melt during cooling and thus have incompatible trace element compositions that were unaffected by chromatographic fractionation (i.e. their infiltration fronts have already passed through the harzburgite).

Unlike plagioclase lherzolite pyroxene, orthopyroxene in the Trinity harzburgite equilibrated with the reacting melt and chromatographically fractionated trace elements. Why are the incompatible trace element fronts predicted in Fig. 9 not observed? The grain-scale concentration gradients in plagioclase lherzolite clinopyroxene (Fig. 5) suggest that REE chromatrographic fronts migrated beyond the lherzolite–plagioclase lherzolite boundary, deep into the plagioclase lherzolite. This is supported by the significant offset of the Ni gradient into the harzburgite. The analysis presented in Fig. 9 suggests $L_e/L_{Ni} > 200$ for REE and HFSE in a harzburgite at mantle relevant melt fractions. These observations suggest that a pervasive melt infiltration event extended over hundreds to thousands of meters away from the dunite source.

Characteristics and origin of the infiltrating melt

The trace element characteristics of the melts from which clinopyroxene crystallized in the dunite, harzburgite, and lherzolite are informative for evaluating the nature of the infiltrating melt. Figure 10 displays calculated REE abundances in melts in equilibrium with clinopyroxene in dunite (green lines) and harzburgite–

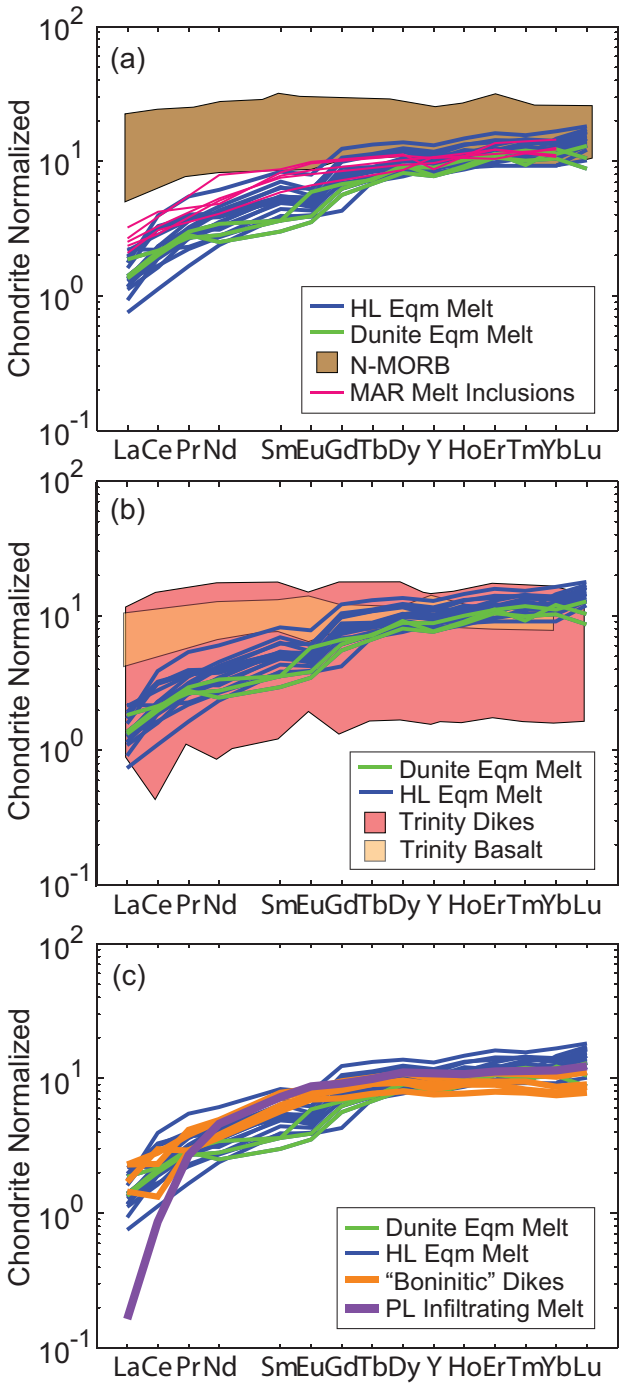

Fig. 10. Melt compositions in equilibrium with Trinity clinopyroxene compared with (a) the global N-MORB suite (PetDB) and olivine-hosted melt inclusions from the Mid-Atlantic Ridge (MAR; Shimizu, 1998), (b) dikes and basalts from the crustal section of the Trinity ophiolite (Brouxel & Lapierre, 1988; Metcalf *et al.*, 2000), (c) four boninitic dikes that cross-cut crustal gabbros at Trinity (Metcalf *et al.*, 2000) and the plagioclase lherzolite-forming infiltrating melt shown in Fig. 7. Equilibrium melt compositions were calculated using the temperature- and composition-dependent partition coefficient model of Sun & Liang (2012) for REE + Y (at 1200°C). The dikes and equilibrium melts are plotted in an extended trace element diagram that compares their Sr, Zr, Ti, and Hf compositions in Supplementary Data Fig. S4.

lherzolite (blue lines) from this study. In terms of their REE patterns, the equilibrium melts are unlike MORB (Fig. 10a), but similar to some rocks from the crustal section of Trinity (Fig. 10b). Trinity basalts have HREE abundances comparable with the equilibrium melts, but with different slopes. Dikes from the crustal section have a much larger compositional range, overlapping the equilibrium melts. Four mafic dikes [samples 978-9, 978-11, P987-47, 986-5 of Metcalf *et al.* (2000)] have REE abundances and LREE depletion similar to the equilibrium melts (orange lines, Fig. 10c; see Supplementary Data Fig. S4 for comparisons of Sr, Zr, Hf and Ti). These dikes cut crustal intrusive complexes at three localities (Bonanza King, Craggy Peak, and Porcupine Lake) and, according Metcalf *et al.* (2000), they have 'boninitic' major element compositions together with trace element abundances suggesting a depleted MORB-type mantle source enriched by subduction-related fluids. Because the dikes cross-cut crustal intrusive rocks they must have formed late in the evolutionary history of the ophiolite, perhaps contemporaneous with the crystallization of the last dunite-hosted melts in the mantle section. These dikes may be related to the melts that crystallized clinopyroxene in the dunite, harzburgite, and lherzolite, although such a connection cannot be confirmed based on trace element patterns alone. Indeed, the similarity between olivine-hosted melt inclusions from the Mid-Atlantic Ridge and the dunite–harzburgite–lherzolite clinopyroxene equilibrium melts (Fig. 10a) suggests that the trace element patterns for melts in equilibrium with the Trinity clinopyroxenes are also present in near-fractional melts of the MORB mantle.

Could the infiltrating melt that formed the plagioclase lherzolite and the DHL-forming melt have originated from a common evolving source; for example, an initially fertile region of the mantle wedge that became depleted owing to extensive hydrous melting? Figure 10c compares the melt from our plagioclase lherzolite formation model (same purple line as in Fig. 7) with Trinity dunite–harzburgite–lherzolite equilibrium melts (green and blue lines). Because the plagioclase lherzolite infiltrating melt is more LREE depleted than the dunite–harzburgite–lherzolite equilibrium melt, no batch or fractional melt of a source that generated the plagioclase lherzolite infiltrating melt is capable of producing LREE concentrations consistent with the dunite–harzburgite–lherzolite equilibrium melts at higher extents of melting. The slope of the plagioclase lherzolite infiltrating melt trace element pattern is model dependent but it should be a good approximation. Thus, the two melts probably originated from unique sources.

IMPLICATIONS FOR MELT MIGRATION IN DUNITE CHANNELS

The concentration gradients we observe (low trace element abundances in dunite grading into higher concentrations in plagioclase lherzolite) are opposite those

present in Oman (i.e. low REE concentrations in harzburgite grading into high REE concentrations in dunite; Supplementary Data Fig. S5), which have been interpreted as facilitating near-fractional melt extraction (Kelemen *et al.*, 1995*a*, 1997). In contrast, at least in the observable geological history, the Trinity dunite channels were a source for local melt infiltration in addition to melt extraction pathways, as previously inferred by Kelemen *et al.* (1992) and Morgan *et al.* (2008).

Globally, the formation of DHL–PL lithological sequences has been attributed to variations in partial melting (e.g. Obata & Nagahara, 1987; Takahashi, 1992), melt–rock reaction and partial melting (e.g. Takazawa *et al.*, 1992, 2000; Lundstrom *et al.*, 2005), or melt–rock reaction alone (e.g. Kelemen, 1990; Kelemen *et al.*, 1992; Piccardo *et al.*, 2007; Morgan *et al.*, 2008; Garrido *et al.*, 2014). Although the details of DHL–PL formation must differ depending on locality (e.g. the tectonic setting, plagioclase lherzolite and infiltrating melt compositions, and *P–T–t* path), the relatively simple melt–rock reaction formation mechanism illustrated in Fig. 8 is a physically viable candidate for forming DHL–PL sequences in general. DHL–PL sequences similar to Trinity have been observed in the Lanzo, Horoman and Ronda peridotites (e.g. Takazawa *et al.*, 1992; Piccardo *et al.*, 2007; Garrido *et al.*, 2014), suggesting that such infiltration events are common. Numerous geochemical studies of ophiolites and abyssal peridotites propose a multi-stage evolutionary process involving partial melting, refertilization, and/or metasomatism (e.g. Elthon, 1992; Kelemen *et al.*, 1992; Ozawa & Shimizu, 1995; Niu, 2004; Brunelli *et al.*, 2006; Collier & Kelemen, 2010; Warren & Shimizu, 2010; Batanova *et al.*, 2011). These infiltration events may be facilitated by melt migration from dunite channels.

What physical mechanisms can cause melt migration from dunite channels into host-rock? Kelemen *et al.* (1995*b*) and Morgan *et al.* (2008) hypothesized that this may occur at the front of a propagating dunite channel, which would develop owing to corner flow beneath a spreading center. With a steady supply of melt from below, a dunite channel oriented at an acute angle to the crust will facilitate flow into the overlying host-rock (e.g. Suhr *et al.*, 2003; Rabinowicz & Ceuleneer, 2005; Baltzell *et al.*, 2015). However, dunite–harzburgite–lherzolite plagioclase lherzolite sequences are generally symmetrical about the dunite (Quick, 1981*a*; Takazawa *et al.*, 1992; Garrido *et al.*, 2014), suggesting that this process may not be relevant to the genesis of most DHL–PL sequences.

Another potential mechanism relates to buoyancy. If a melt-bearing dunite channel had a low-permeability cap (e.g. from *in situ* crystallization of dunite-hosted melt near the top of the channel) the underlying column of melt would apply a pressure in all directions proportional to its height and melt would flow laterally into the dunite channel host-rock. Buoyancy-driven dunite channel host-rock infiltration could be especially important at slow and ultra-slow spreading centers, which are thought to have a relatively deep conductive thermal regime (e.g. Shen & Forsyth, 1992; Cannat, 1996; Kelemen *et al.*, 2007; Collier & Kelemen, 2010; Conley & Dunn, 2011).

Recent numerical simulations predict melt focusing along dunite channel–host-rock contacts owing to feedbacks between melt–rock reaction and compaction (Aharonov *et al.*, 1995; Spiegelman *et al.*, 2001; Spiegelman & Kelemen, 2003; Liang *et al.*, 2010, 2011; Schiemenz *et al.*, 2010). The predictions are consistent with geochemical concentration gradients observed within some dunite channels, and the crystallization of dunite channel hosted melt cumulates along some dunite channel walls (e.g. Suhr *et al.*, 2003; Braun, 2004; Maaløe, 2005; Morgan *et al.*, 2008; Dygert & Liang, 2010; Batanova *et al.*, 2011). Melt focusing within dunites may make buoyant infiltration of the host-rock easier by positioning melt along the dunite–host-rock contact prior to infiltration.

Another mechanism capable of causing melt infiltration is the formation of nonlinear porosity waves, which are predicted to develop during melt migration beneath spreading centers owing to feedbacks between dissolution, compaction and upwelling (Hesse *et al.*, 2011; Liang *et al.*, 2011). In the numerical simulations in which they were observed, these compaction–dissolution waves develop a significant component of lateral melt transport, allowing melt to flow from dunite into adjacent harzburgite and through harzburgite into a nearby dunite (see Liang *et al.*, 2011, fig. 2). If extensive infiltration of mantle peridotite by dunite-hosted basaltic melts is a commonly occurring process, crystallization of significant volumes of melt directly in the mantle may be expected (e.g. Cannat, 1996; Lenoir *et al.*, 2001; Bodinier *et al.*, 2008; Soustelle *et al.*, 2009; Collier & Kelemen, 2010; Conley & Dunn, 2011; Sleep & Warren, 2014). The importance of such a process to global geochemical cycles depends on the volume of pervasive mantle infiltration and its frequency in general. Evaluating the impact of this process requires new, large-scale geochemical-spatial investigations of ophiolitic peridotites.

CONCLUSIONS

We measured trace elements across a dunite–harzburgite–lherzolite–plagioclase lherzolite sequence within the Trinity ophiolite. Clinopyroxene in the dunite, harzburgite, and lherzolite has relatively low REE abundances similar to other suprasubduction-zone ophiolites and plagioclase-free abyssal peridotites. Plagioclase lherzolite clinopyroxenes have high REE concentrations and steep LREE-depleted patterns, typical of ophiolitic plagioclase lherzolites.

We modeled the formation of plagioclase lherzolite assuming melt infiltration and 100% crystallization of the trapped melt. This simple model accounts for the major and trace element compositions of the resultant plagioclase lherzolite. Based on spatial-geochemical,

textural, and geological observations, we propose a two-stage history of evolution preserved at the Trinity outcrop: (1) formation of plagioclase lherzolite by magmatic impregnation of a depleted, residual harzburgite; (2) formation of a pyroxene-free dunite channel in the plagioclase lherzolite, coupled with pervasive infiltration of dunite-sourced melt into the plagioclase lherzolite wall-rock, with concomitant melt–rock reaction between plagioclase lherzolite and the infiltrating, pyroxene- and plagioclase-undersaturated melt.

Significantly, the Trinity outcrop demonstrates that dunite channels can be sources of melt infiltration as well as extraction pathways as proposed by Kelemen *et al.* (1992) and Morgan *et al.* (2008). Similar dunite–harzburgite–lherzolite–plagioclase lherzolite sequences observed at ophiolites around the world may reveal that dunite channel-facilitated melt infiltration is common in the upper mantle. Infiltration of wall-rock by dunite-hosted melts may be facilitated by corner flow, buoyancy-driven lateral percolation, compaction, nonlinear porosity waves, or a combination of these mechanisms.

FUNDING

This work was supported in part by National Science Foundation grants EAR-0911501, OCE-1156706 and EAR-1220076, and by Rhode Island Space Grant and Brown University Dissertation Fellowships to N.D., as well as a Jackson School of Geosciences Postdoctoral Fellowship.

ACKNOWLEDGEMENTS

We thank Katherine Kelley for her assistance with trace element analyses, the late Joe Devine for his help with thin section mapping, and Jessica Warren, Elisabetta Rampone, and Carlos Garrido for thoughtful reviews that significantly improved this paper.

SUPPLEMENTARY DATA

Supplementary data for this paper are available at *Journal of Petrology* online.

REFERENCES

Aharonov, E., Whitehead, J. A., Kelemen, P. B. & Spiegelman, M. (1995). Channeling instability of upwelling melt in the mantle. *Journal of Geophysical Research* **100**, 20433–20450.

Asimow, P. D. & Ghiorso, M. S. (1998). Algorithmic modifications extending MELTS to calculate subsolidus phase relations. *American Mineralogist* **83**, 1127–1132.

Asimow, P. D. & Stolper, E. M. (1999). Steady-state mantle–melt interactions in one dimension: I. Equilibrium transport and melt focusing. *Journal of Petrology* **40**, 475–494.

Baltzell, C., Parmentier, E. M., Liang, Y. & Tirupathi, S. (2015). A high-order numerical study of reactive dissolution in an upwelling heterogeneous mantle: 2. Effect of shear deformation. *Geochemistry, Geophysics, Geosystems* **16**, doi:10.1002/2015GC006038.

Barth, M. G., Mason, P. R. D., Davies, G. R., Dijkstra, A. H. & Drury, M. R. (2003). Geochemistry of the Othris ophiolite, Greece: Evidence for refertilization? *Journal of Petrology* **44**, 1759–1785.

Batanova, V. G., Belousov, I. A., Savelieva, G. N. & Sobolev, A. V. (2011). Consequences of channelized and diffuse melt transport in supra-subduction zone mantle: Evidence from the Voykar Ophiolite (Polar Urals). *Journal of Petrology* **52**, 2483–2521.

Bindeman, I. N., Davis, A. M. & Drake, M. J. (1998). Ion microprobe study of plagioclase–basalt partition experiments at natural concentration levels of trace elements. *Geochimica et Cosmochimica Acta* **62**, 1175–1193.

Bizimis, M., Salters, V. J. M. & Bonatti, E. (2000). Trace and REE content of clinopyroxenes from supra-subduction zone peridotites. Implications for melting and enrichment processes in island arcs. *Chemical Geology* **165**, 67–85.

Blundy, J. D. & Wood, B. J. (1994). Prediction of crystal–melt partition coefficients from elastic moduli. *Nature* **372**, 452–454.

Bodinier, J. L. & Godard, M. (2003). Orogenic, ophiolitic, and abyssal peridotites. In: Carlson, R. W. (ed.) *Treatise on Geochemistry*, 2. Amsterdam: Elsevier, pp. 103–170.

Bodinier, J. L., Vasseur, G., Vernières, J., Dupuy, C. & Fabriès, J. (1990). Mechanisms of mantle metasomatism: geochemical evidence from the Lherz orogenic peridotite. *Journal of Petrology* **31**, 597–628.

Bodinier, J. L., Menzies, M. A. & Thirlwall, M. F. (1991). Continental to oceanic mantle transition–REE and Sr–Nd isotopic geochemistry of the Lanzo Lherzolite Massif. *Journal of Petrology, Special Lherzolites Issue*, 191–210.

Bodinier, J. L., Garrido, C. J., Chanefo, I., Bruguier, O. & Gervilla, F. (2008). Origin of pyroxenite–peridotite veined mantle by refertilization reactions: Evidence from the Ronda peridotite (southern Spain). *Journal of Petrology* **49**, 999–1025.

Bonatti, E., Honnorez, J. & Ferrara, G. (1970). Equatorial Mid-Atlantic Ridge: petrologic and Sr isotopic evidence for an alpine-type rock assemblage. *Earth and Planetary Science Letters* **9**, 247–256.

Bonatti, E., Peyve, A., Kepezhinskas, P., Kurentsova, N., Seyler, M., Skolotnev, S. & Udintsev, G. (1992). Upper mantle heterogeneity below the Mid-Atlantic Ridge, 0°–15°N. *Journal of Geophysical Research* **97**, 4461–4476.

Bonatti, E., Seyler, M., Sushevskaya, N. (1993). A cold suboceanic mantle belt at the Earth's equator. *Science* **261**, 315–320.

Borghini, G., Rampone, E., Crispini, L., De Ferrari, R. & Godard, M. (2007). Origin and emplacement of ultramafic–mafic intrusions in the Erro–Tobbio mantle peridotite (Ligurian Alps, Italy). *Lithos* **94**, 210–229.

Borghini, G., Fumagalli, P. & Rampone, E. (2010). The stability of plagioclase in the upper mantle: subsolidus experiments on fertile and depleted lherzolite. *Journal of Petrology* **51**, 229–254.

Boudier, F. & Nicolas, A. (1985). Harzburgite and lherzolite subtypes in ophiolitic and oceanic environments. *Earth and Planetary Science Letters* **76**, 84–92.

Boudier, F., Le Sueur, E. & Nicolas, A. (1989). Structure of an atypical ophiolite: The Trinity complex, eastern Klamath Mountains, California. *Geological Society of America Bulletin* **101**, 820–833.

Braun, M. G. (2004). Petrologic and microstructural constraints on focused melt transport in dunites and the rheology of the shallow mantle. PhD thesis, Massachusetts Institute of Technology, Cambridge, MA.

Brouxel, M. & Lapierre, H. (1988). Geochemical study of an early Paleozoic island-arc–back-arc basin system. Part 1: The Trinity Ophiolite (northern California). *Geological Society of America Bulletin* **100**, 1111–1119.

Brunelli, D. & Seyler, M. (2010). Asthenospheric percolation of alkaline melts beneath the St. Paul region (Central Atlantic Ocean). *Earth and Planetary Science Letters* **289**, 393–405.

Brunelli, D., Seyler, M., Cipriani, A. Ottolini, L. & Bonatti, E. (2006). Discontinuous melt extraction and weak refertilization of mantle peridotites at the Vema lithospheric section (Mid-Atlantic Ridge). *Journal of Petrology* **47**, 745–771.

Cannat, M. (1996). How thick is the magmatic crust at slow spreading oceanic ridges? *Journal of Geophysical Research* **101**, 2847–2857.

Cannat, M. & Lécuyer, C. (1991). Ephemeral magma chambers in the Trinity peridotite, northern California. *Tectonophysics* **186**, 313–328.

Ceuleneer, G. & Le Sueur, E. (2008). The Trinity ophiolite (California): the strange association of fertile mantle peridotite with ultra-depleted crustal cumulates. *Bulletin de la Société Géologique de France* **179**, 503–518.

Cherniak, D. J. & Liang, Y. (2007). Rare earth element diffusion in natural enstatite. *Geochimica et Cosmochimica Acta* **71**, 1324–1340.

Cherniak, D. J. & Liang, Y. (2012). Ti diffusion in natural pyroxene. *Geochimica et Cosmochimica Acta* **98**, 31–47.

Collier, M. L. & Kelemen, P. B. (2010). The case for reactive crystallization at mid-ocean ridges. *Journal of Petrology* **51**, 1913–1940.

Conley, M. M. & Dunn, R. A. (2011). Seismic shear wave structure of the uppermost mantle beneath the Mohns Ridge. *Geochemistry, Geophysics, Geosystems* **12**, doi:10.1029/2011GC003792.

Daines, M. J. & Kohlstedt, D. L. (1994). The transition from porous to channelized flow due to melt/rock reaction during melt migration. *Geophysical Research Letters* **21**, 145–148.

Dick, H. J. B. (1989). Abyssal peridotites, very slow spreading ridges and ocean ridge magmatism. In: Saunders, A. D. & Norry, M. J. (eds) *Magmatism in the Ocean Basins. Geological Society, London, Special Publication* **42**, 71–105.

Dick, H. J. B., Lissenberg, C. J. & Warren, J. M. (2010). Mantle melting, melt transport, and delivery beneath a slow-spreading ridge: The Paleo-MAR from 23°15′N to 23°45′N. *Journal of Petrology* **51**, 425–467.

Dijkstra, A. H., Barth, M. G., Drury, M. R., Mason, P. R. D. & Vissers, R. L. M. (2001). Diffuse porous melt flow and melt–rock reaction in the mantle lithosphere at a slow spreading ridge: A structural petrology and LA-ICP-MS study of the Othris Peridotite Massif (Greece). *Geochemistry, Geophysics, Geosystems* **4**, doi:10.1029/2001GC000278.

Drake, M. & Weill, D. (1975). Partition of Sr, Ba, Ca, Y, Eu^{2+}, Eu^{3+}, and other REE between plagioclase feldspar and magmatic liquid: an experimental study. *Geochimica et Cosmochimica Acta* **39**, 689–712.

Dygert, N. & Liang, Y. (2010). Compaction driven melt localization in dunites and associated rocks in the mantle: field observations and numerical experiments. *American Geophysical Union Fall Meeting*, T23A–2229 (abstract).

Dygert, N. & Liang, Y. (2015). Temperatures and cooling rates recorded in REE in coexisting pyroxenes in ophiolitic and abyssal peridotites. *Earth and Planetary Science Letters* **420**, 151–161.

Elthon, D. (1992). Chemical trends in abyssal peridotites: refertilization of depleted suboceanic mantle. *Journal of Geophysical Research* **97**, 9015–9025.

Garrido, C. J. & Bodinier, J. L. (1999). Diversity of mafic rocks in the Ronda Peridotite: evidence for pervasive melt–rock reaction during heating of subcontinental lithosphere by upwelling asthenosphere. *Journal of Petrology* **40**, 729–754.

Garrido, C. J., Bodinier, J. L. & Alard, O. (2000). Incompatible trace element partitioning and residence in anhydrous spinel peridotites and websterites from the Ronda orogenic peridotite. *Earth and Planetary Science Letters* **181**, 341–358.

Garrido, C. J., Hidas, K., Bodinier, J. L., Marchesi, C., Gervilla, F., Remaidi, M. & Acosta-Vigil, A. (2014). Channeling of reactive porous flow in the subcontinental lithospheric mantle: lherzolite–harzburgite–dunite layered peridotite bodies of the Ronda massif (Betic Cordillera, S-Spain). In: *6th International Lherzolite Conference* (abstract).

Girardeau, J. & Francheteau, J. (1993). Plagioclase-wehrlites and peridotites on the East Pacific Rise (Hess Deep) and the Mid-Atlantic Ridge (DSDP site 334): Evidence for magma percolation in the oceanic upper mantle. *Earth and Planetary Science Letters* **115**, 137–149.

Godard, M., Bodinier, J. L. & Vasseur, G. (1995). Effects of mineralogical reactions on trace element redistributions in mantle rocks during percolation processes: A chromatographic approach. *Earth and Planetary Science Letters* **133**, 449–461.

Gruau, G., Lecuyer, C., Bernard-Griffiths, J. & Morin, N. (1991). Origin and petrogenesis of the Trinity ophiolite complex (California): New constraints from REE and Nd isotope data. *Journal of Petrology, Special Volume 2*, 229–242.

Gruau, G., Bernard-Griffiths, J., Lécuyer, C., Henin, O., Macé, J. & Cannat, M. (1995). Extreme Nd isotopic variation in the Trinity Ophiolite Complex and the role of melt/rock reactions in the oceanic lithosphere. *Contributions to Mineralogy and Petrology* **121**, 337–350.

Gruau, G., Bernard-Griffiths, J. & Lecuyer, C. (1998). The origin of U-shaped rare earth patterns in ophiolite peridotites: Assessing the role of secondary alteration and melt/rock reaction. *Geochimica et Cosmochimica Acta* **62**, 3545–3560.

Guarnieri, L., Nakamura, E., Piccardo, G. B., Sakaguchi, C., Shimizu, N., Vannucci, R. & Zanetti, A. (2012). Petrology, trace element and Sr, Nd, Hf isotope geochemistry of the North Lanzo Peridotite Massif (Western Alps, Italy). *Journal of Petrology* **53**, 2259–2306.

Hesse, M. A., Schiemenz, A. R., Liang, Y. & Parmentier, E. M. (2011). Compaction–dissolution waves in an upwelling mantle column. *Geophysical Journal International* **187**, 1057–1075.

Hofmann, A. (1972). Chromatographic theory of infiltration metasomatism and its application to feldspars. *American Journal of Science* **272**, 69–90.

Jacobsen, S. B., Quick, J. E. & Wasserburg, G. J. (1984). A Nd and Sr isotopic study of the Trinity peridotite; implications for mantle evolution. *Earth and Planetary Science Letters* **68**, 361–378.

Kelemen, P. B. (1986). Assimilation of ultramafic rock in subduction-related magmaic arcs. *Journal of Geology* **94**, 829–843.

Kelemen, P. B. (1990). Reaction between ultramafic rock and fractionating basaltic magma I. Phase relations, the origin of calc-alkaline magma series, and the formation of discordant dunite. *Journal of Petrology* **31**, 51–98.

Kelemen, P. B., Dick, H. J. B. & Quick, J. E. (1992). Formation of harzburgite by pervasive melt/rock reaction in the upper mantle. *Nature* **358**, 635–641.

Kelemen, P. B., Shimizu, N. & Salters, V. J. M. (1995*a*). Extraction of mid-ocean-ridge basalt from the upwelling mantle by focused flow of melt in dunite channels. *Nature* **375**, 747–753.

Kelemen, P. B., Whitehead, J. A., Aharonov, E. & Jordahl, K. A. (1995*b*). Experiments on flow focusing in soluble porous media, with applications to melt extraction from the mantle. *Journal of Geophysical Research* **100**, 475–496.

Kelemen, P. B., Hirth, G., Shimizu, N., Spiegelman, M. & Dick, H. J. B. (1997). A review of melt migration processes in the adiabatically upwelling mantle beneath oceanic spreading ridges. *Philosophical Transactions of the Royal Society of London* **355**, 238–318.

Kelemen, P. B., Hanghøj, K. & Greene, A. R. (2003). One view of the geochemistry of subduction-related magmatic arcs, with an emphasis on primitive andesite and lower crust. In: Rudnick, R. (ed.) *Treatise on Geochemistry, 3*, 1st edn. Amsterdam: Elsevier, pp. 593–659.

Kelemen, P. G., Kikawa, E., Miller, D. J., et al. (2007). Leg 209 summary: Processes in a 20-km-thick conductive boundary layer beneath the Mid-Atlantic Ridge, 14–16°N. In: Kelemen, P. B., Kikawa, E. & Miller, D. J. (eds) *Proceedings of the Ocean Drilling Program, Scientific Results, 209*. College Station, TX: Ocean Drilling Program, pp. 1–33.

Kelemen, P. B., Hanghøj, K. & Greene, A. R. (2014). One view of the geochemistry of subduction-related magmatic arcs, with an emphasis on primitive andesite and lower crust. In: Rudnick, R. (ed.) *Treatise on Geochemistry, 4*, 2nd edn. Amsterdam: Elsevier, pp. 749–806.

Kelley, K. A., Plank, T., Ludden, J. & Staudigel, H. (2003). Composition of altered oceanic crust at ODP Sites 801 and 1149. *Geochemistry, Geophysics, Geosystems* **4**, 8910.

Kubo, K. (2002). Dunite formation processes in highly depleted peridotite: case study of the Iwanaidake Peridotite, Hokkaido, Japan. *Journal of Petrology* **43**, 423–488.

Lambart, S., Laporte, D. & Schiano, P. (2009). An experimental study of focused magma transport and basalt–peridotite interactions beneath mid-ocean ridges: implications for the generation of primitive MORB compositions. *Contributions to Mineralogy and Petrology* **157**, 429–451.

Lenoir, X., Garrido, C., Bodinier, J., Dautria, J. & Gervilla, F. (2001). The recrystallization front of the Ronda peridotite: Evidence for melting and thermal erosion of subcontinental lithospheric mantle beneath the Alboran basin. *Journal of Petrology* **42**, 141–158.

Le Sueur, E., Boudier, F., Cannat, M., Ceuleneer, G. & Nicolas, A. (1984). The Trinity mafic–ultramafic complex: first results of the structural study of an untypical ophiolite. *Ofioliti* **9**, 487–498.

Liang, Y., Schiemenz, A., Hesse, M. A., Parmentier, E. M. & Hesthaven, J. S. (2010). High-porosity channels for melt migration in the mantle: Top is the dunite and bottom is the harzburgite and lherzolite. *Geophysical Research Letters* **37**, L15306.

Liang, Y., Schiemenz, A., Hesse, M. A. & Parmentier, E. M. (2011). Waves, channels, and the preservation of chemical heterogeneities during melt migration in the mantle. *Geophysical Research Letters* **38**, L20308.

Lindsley-Griffin, N. (1977). The Trinity ophiolite, Klamath Mountains, California. *Oregon Department of Geology and Mineral Industries Bulletin* **95**, 107–120.

Lindsley-Griffin, N. (1991). The Trinity complex: A polygenetic ophiolitic assemblage. In: Cooper, J. D. & Stevens, C. H. (eds) *Paleozoic Paleogeography of the Western United States—II. Pacific Section, Society for Sedimentary Geology* **67**, 589–607.

Liu, C. A., Wu, F. Y., Wilde, S. A., Yu, L. J. & Li, J. L. (2010). Anorthitic plagioclase and pargasitic amphibole in mantle peridotites from the Yungbwa ophiolite (southwestern Tibetan Plateau) formed by hydrous melt metasomatism. *Lithos* **114**, 413–422.

Lo Cascio, M. (2008). Kinetics of partial melting and melt–rock reaction in the Earth's mantle. PhD thesis, Brown University.

Lundstrom, C. C., Chaussidon, M., Hsui, A. T., Kelemen, P. & Zimmerman, M. (2005). Observations of Li isotopic variations in the Trinity Ophiolite: Evidence for isotopic fractionation by diffusion during mantle melting. *Geochimica et Cosmochimica Acta* **69**, 735–751.

Maaløe, S. (2005). The dunite bodies, websterite and orthopyroxenite dikes of the Leka ophiolite complex, Norway. *Mineralogy and Petrology* **85**, 163–204.

Menzies, M. & Allen, C. (1974). Plagioclase lherzolite–residual mantle relationships within two eastern Mediterranean ophiolites. *Contributions to Mineralogy and Petrology* **45**, 197–213.

Mercier, J.-C. C. & Nicolas, A. (1975). Textures and fabrics of upper-mantle peridotites as illustrated by xenoliths from basalts. *Journal of Petrology* **16**, 454–487.

Metcalf, R. V., Wallin, E. T., Willse, K. R. & Muller, E. R. (2000). In: Dilek, Y. (ed.) *Ophiolites and Oceanic Crust: New Insights from Field Studies and the Ocean Drilling Program*. Geology and geochemistry of the ophiolitic Trinity Terrane, California: Evidence of middle Paleozoic depleted suprasubduction zone magmatism in a proto-arc setting. Geological Society of America, Special Paper **349**, doi:10.1130/0-8137-2349-3.403.

Morgan, Z. (2006). Kinetics of melt–rock reaction with applications to melt transport in the Earth's mantle and the lunar crust. PhD thesis, Brown University, Providence, RI.

Morgan, Z. & Liang, Y. (2003). An experimental and numerical study of the kinetics of harzburgite reactive dissolution with applications to dunite dike formation. *Earth and Planetary Science Letters* **214**, 59–74.

Morgan, Z. & Liang, Y. (2005). An experimental study of the kinetics of lherzolite reactive dissolution with applications to melt channel formation. *Contributions to Mineralogy and Petrology* **150**, 269–385.

Morgan, Z., Liang, Y. & Kelemen, P. (2008). Significance of the concentration gradients associated with dunite bodies in the Josephine and Trinity ophoilites. *Geochemistry, Geophysics, Geosystems* **9**, doi:10.1029/2008GC001954.

Müntener, O., Manatschal, G., Desmurs, L. & Pettke, T. (2010). Plagioclase peridotites in ocean–continent transitions: refertilized mantle domains generated by melt stagnation in the shallow mantle lithosphere. *Journal of Petrology* **51**, 255–294.

Navon, O. & Stolper, E. (1987). Geochemical consequences of melt percolation: The upper mantle as a chromatographic column. *Journal of Geology* **95**, 285–307.

Nicolas, A. (1986). A melt extraction model based on structural studies in mantle peridotites. *Journal of Petrology* **27**, 999–1022.

Nicolas, A. & Dupuy, C. (1984). Origin of ophiolitic and oceanic lherzolites. *Tectonophysics* **110**, 177–187.

Niu, Y. (2004). Bulk-rock major and trace element compositions of abyssal peridotites: implications for mantle melting, melt extraction and post-melting processes beneath mid-ocean ridges. *Journal of Petrology* **45**, 2423–2458.

Niu, Y. & Hékinian, R. (1997). Basaltic liquids and harzburgitic residues in the Garrett Transform: a case study at fast-spreading ridges. *Earth and Planetary Science Letters* **146**, 243–258.

Obata, M. & Nagahara, N. (1987). Layering of alpine-type peridotite and the segregation of partial melt in the upper mantle. *Journal of Geophysical Research* **92**, 3467–3474.

Ozawa, K. & Shimizu, N. (1995). Open-system melting in the upper mantle: Constraints from the Hayachine–Miyamori ophiolite, northeast Japan. *Journal of Geophysical Research* **100**, 22315–22335.

Pagé, P., Bédard, J. H., Schroetter, J. M. & Tremblay, A. (2008). Mantle petrology and mineralogy of the Thetford Mines Ophiolite Complex. *Lithos* **100**, 255–292.

Pec, M., Holtzman, B. K., Zimmerman, M. & Kohlstedt, D. L. (2015). Reaction infiltration instabilities in experiments on partially molten mantle rocks. *Geology* **43**, 575–578.

Petry, C., Chakraborty, S. & Palme, H. (2004). Experimental determination of Ni diffusion coefficients in olivine and their dependence on temperature, compositions, oxygen fugacity, and crystallographic orientation. *Geochimica et Cosmochimica Acta* **68**, 4179–4188.

Piccardo, G. B., Zanetti, A. & Müntener, O. (2007). Melt/peridotite interaction in the Southern Lanzo peridotite: Field, textural and geochemical evidence. *Lithos* **94**, 181–209.

Prinzhofer, A. & Allègre, C. J. (1985). Residual peridotites and the mechanisms of partial melting. *Earth and Planetary Science Letters* **74**, 251–265.

Quick, J. E. (1981*a*). The origin and significance of large, tabular dunite bodies in the Trinity Peridotite, northern California. *Contributions to Mineralogy and Petrology* **78**, 413–422.

Quick, J. E. (1981*b*). Petrology and petrogenesis of the Trinity Peridotite, an upper mantle diapir in the eastern Klamath Mountains, northern California. *Journal of Geophysical Research* **86**, 11837–11863.

Quick, J. E. & Gregory, R. T. (1995). Significance of melt–wall rock reaction: A comparative anatomy of three ophiolites. *Journal of Geology* **103**, 187–198.

Rabinowicz, M. & Ceuleneer, G. (2005). The effect of sloped isotherms on melt migration in the shallow mantle: a physical and numerical model based on observations in the Oman ophiolite. *Earth and Planetary Science Letters* **229**, 231–246.

Rampone, E., Bottazzi, P. & Ottolini, L. (1991). Complementary Ti and Zr anomalies in orthopyroxene and clinopyroxene from mantle peridotites. *Nature* **354**, 518–520.

Rampone, E., Piccardo, G. B., Vannucci, R., Bottazzi, P. & Ottolini, L. (1993). Subsolidus reactions monitored by trace element partitioning: the spinel- to plagioclase-facies transition in mantle peridotites. *Contributions to Mineralogy and Petrology* **115**, 1–17.

Rampone, E., Piccardo, G. B., Vannucci, R. & Bottazzi, P. (1997). Chemistry and origin of trapped melts in ophiolitic peridotites. *Geochimica et Cosmochimica Acta* **61**, 4557–4569.

Rampone, E., Piccardo, G. B. & Hofmann, A. W. (2008). Multistage melt–rock interaction in the Mt. Maggiore (Corsica, France) ophiolitic perdiotites: microstructural and geochemical evidence. *Contributions to Mineralogy and Petrology* **156**, 453–475.

Saper, L. & Liang, Y. (2014). Formation of plagioclase-bearing peridotite and plagioclase-bearing wehrlite and gabbro suite through reactive crystallization: an experimental study. *Contributions to Mineralogy and Petrology* **167**, doi:10.1007/s00410-014-0985-7.

Schiemenz, A., Liang, Y. & Parmentier, E. M. (2010). A high-order numerical study of reactive dissolution in an upwelling heterogeneous mantle: I. Channelization, channel lithology, and channel geometry. *Geophysical Journal International* **186**, 641–664.

Seyler, M. & Bonatti, E. (1997). Regional-scale melt–rock interaction in lherzolitic mantle in the Romanche Fracture Zone (Atlantic Ocean). *Earth and Planetary Science Letters* **146**, 273–287.

Shen, Y. & Forsyth, D. W. (1992). The effects of temperature- and pressure-dependent viscosity on three-dimensional passive flow of the mantle beneath a ridge–transform system. *Journal of Geophysical Research* **97**, 19717–19728.

Shimizu, N. (1998). The geochemistry of olivine-hosted melt inclusions in a FAMOUS basalt ALV519-4-1. *Physics of the Earth and Planetary Interiors* **107**, 183–201.

Sleep, N. H. & Warren, J. W. (2014). Effect of latent heat of freezing on crustal generation at low spreading rates. *Geochemistry, Geophysics, Geosystems* **15**, 3161–3174.

Smith, P. M. & Asimow, P. D. (2005). Adiabat_1ph: A new public front-end to the MELTS, pMELTS, and pHMELTS models. *Geochemistry, Geophysics, Geosystems* **6**, doi:10.1029/2004GC000816.

Soustelle, V., Tommasi, A., Bodinier, J. L., Garrido, C. J. & Vauchez, A. (2009). Deformation and reactive melt transport in the mantle lithosphere above a large-scale partial melting domain: the Ronda Peridotite massif, southern Spain. *Journal of Petrology* **50**, 1235–1266.

Sparks, D. W. & Parmentier, E. M. (1991). Melt extraction from the mantle beneath spreading centers. *Earth and Planetary Science Letters* **105**, 368–377.

Sparks, J. (2011). *LASY BOY. An Excel program for processing ICP-MS data*. Boston University.

Spiegelman, M. & Kelemen, P. B. (2003). Extreme chemical variability as a consequence of channelized melt transport. *Geochemistry, Geophysics, Geosystems* **4**, doi:10.1029/2002GC000336.

Spiegelman, M., Kelemen, P. B. & Aharonov, E. (2001). Causes and consequences of flow organization during melt transport: The reaction infiltration instability in compactible media. *Journal of Geophysical Research* **106**, 2061–2077.

Spray, J. G. (1982). Mafic segregations in ophiolite mantle sequences. *Nature* **299**, 524–528.

Suhr, G., Hellebrand, E., Snow, J. E., Seck, H. A. & Hofmann, A. W. (2003). Significance of large, refractory dunite bodies in the upper mantle of the Bay of Islands Ophiolite. *Geochemistry, Geophysics, Geosystems* **4**, doi:10.1029/2001GC000277.

Sun, C. & Liang, Y. (2012). Distribution of REE between clinopyroxene and basaltic melt along a mantle adiabat: effects of major element composition, water, and temperature. *Contributions to Mineralogy and Petrology* **163**, 807–823.

Takahashi, N. (1992). Evidence for melt segregation towards fractures in the Horoman mantle peridotite complex. *Nature* **359**, 52–55.

Takazawa, E., Frey, F. A., Shimizu, N., Obata, M. & Bodinier, J. L. (1992). Geochemical evidence for melt migration and reaction in the upper mantle. *Nature* **359**, 55–58.

Takazawa, E., Frey, F., Shimizu, N. & Obata, M. (1996). Evolution of the Horoman Peridotite (Hokkaido, Japan): Implications from pyroxene compositions. *Chemical Geology* **134**, 3–266.

Takazawa, E., Frey, F. A., Shimizu, N. & Obata, M. (2000). Whole rock compositional variations in an upper mantle peridotite (Horoman, Hokkaido, Japan): Are they consistent with a partial melting process? *Geochimica et Cosmochimica Acta* **64**, 695–716.

Tartarotti, P., Susini, S., Nimis, P. & Ottolini, L. (2002). Melt migration in the upper mantle along the Romanche Fracture Zone (Equatorial Atlantic). *Lithos* **63**, 125–149.

Tursack, E. & Liang, Y. (2011). A comparative study of melt–rock reactions in the mantle: laboratory dissolution experiments and geological field observations. *Contributions to Mineralogy and Petrology* **163**, 861–876.

Van den Bleeken, G., Müntener, O. & Ulmer, P. (2010). Reaction processes between tholeiitic melt and residual peridotite in the uppermost mantle: an experimental study at 0·8 GPa. *Journal of Petrology* **51**, 153–183.

Van Orman, J. A., Grove, T. L. & Shimizu, N. (2001). Rare earth element diffusion in diopside: influence of temperature, pressure, and ionic radius, and an elastic model for diffusion in silicates. *Contributions to Mineralogy and Petrology* **141**, 687–703.

Varfalvy, V., Hébert, R. & Bédard, J. H. (1996). Interactions between melt and upper-mantle peridotites in the North Arm Mountain massif, Bay of Islands ophiolite, Newfoundland, Canada: Implications for the genesis of boninitic and related magmas. *Chemical Geology* **129**, 71–90.

Wallin, E. T. & Metcalf, R. V. (1998). Supra-subduction zone ophiolite formed in an extensional forearc: Trinity Terrane, Klamath Mountains, California. *Journal of Geology* **106**, 591–608.

Wallin, E. T., Lindsley-Griffin, N. & Griffin, J. R. (1991). Overview of early Paleozoic magmatism in the eastern Klamath Mountains, California: An isotopic perspective. In: Cooper, J. D. & Stevens, C. H. (eds) *Paleozoic Paleogeography of the Western United States—II. Pacific Section, Society for Sedimentary Geology* **67**, 581–588.

Wallin, E. T., Coleman, D. S., Lindsley-Griffin, N. & Potter, A. W. (1995). Silurian plutonism in the Trinity terrane (Neoproterozoic and Ordovician), Klamath Mountains, California, USA. *Tectonics* **14**, 1007–1013.

Wang, C., Liang, Y., Xu, W. & Dygert, N. (2013). Effect of melt composition on basalt and peridotite interaction: laboratory dissolution experiments with applications to mineral compositional variations in mantle xenoliths from the North China Craton. *Contributions to Mineralogy and Petrology* **166**, 1469–1488.

Warren, J. M. (2016). Global variations in abyssal peridotite compositions. *Lithos* **248–251**, 193–219.

Warren, J. M. & Shimizu, N. (2010). Cryptic variations in abyssal peridotite compositions: evidence for shallow-level melt infiltration in the oceanic lithosphere. *Journal of Petrology* **51**, 395–423.

Warren, J. M., Shimizu, N., Sakaguchi, C., Dick, H. J. B. & Nakamura, E. (2009). An assessment of upper mantle heterogeneity based on abyssal peridotite isotopic compositions. *Journal of Geophysical Research* **114**, B12203.

Wood, B. J. & Blundy, J. D. (2003). Trace element partitioning under crustal and uppermost mantle conditions: The influences of ionic radius, cation charge, pressure, and temperature. In: Carlson, R. W. (ed.) *Treatise on Geochemistry, 2* Amsterdam: Elseveir, 395–424.

Workman, R. K. & Hart, S. R. (2005). Major and trace element composition of the depleted MORB mantle (DMM). *Earth and Planetary Science Letters* **231**, 53–72.

Zhou, M. F., Robinson, P. T., Malpas, J., Edwards, S. J. & Qi, L. (2005). REE and PGE geochemical constraints on the formation of dunites in the Luobusa Ophiolite, southern Tibet. *Journal of Petrology* **46**, 615–639.